

EVOLUTION OF A PROTOBINARY: ACCRETION RATES OF THE PRIMARY AND SECONDARY

YASUHIRO OCHI,^{1,2} KANAKO SUGIMOTO,^{1,2} AND TOMOYUKI HANAWA^{1,3}

Received 2004 August 6; accepted 2005 January 4

ABSTRACT

We reexamine accretion onto a protobinary based on two-dimensional numerical simulations with high spatial resolution. We focus our attention on the ratio of the primary and secondary accretion rates. Fifty-eight models are made for studying the dependence of the accretion rates on the specific angular momentum of infalling gas j_{inf} , the mass ratio of the binary q , and the sound speed c_s . When j_{inf} is small, the binary accretes the gas mainly through two channels (type I): one through the Lagrange point L2 and the other through L3. When j_{inf} is large, the binary accretes the gas only through the L2 point (type II). The primary accretes more than the secondary in both the cases, although the L2 point is closer to the secondary. After flowing through the L2 point, the gas flows halfway around the secondary and through the L1 point to the primary. Only a small amount of gas flows back to the secondary, and the rest forms a circumstellar ring around the primary. The boundary between types I and II depends on q . When j_{inf} is very large, the accretion begins after several rotations (type III). The beginning of the accretion is later when j_{inf} is larger and c_s is smaller. Our result that the primary accretion rate is higher for a large j_{inf} is qualitatively different from results of earlier simulations. The difference is mainly due to limited spatial resolution and large numerical viscosity in the numerical simulations thus far.

Subject headings: accretion, accretion disks — hydrodynamics — methods: numerical — stars: formation — stars: pre-main-sequence

1. INTRODUCTION

Stars acquire most of their mass through accretion in the protostellar phase (see, e.g., Hartmann 1998; Larson 2003). The accretion is most likely through a circumstellar disk, since each component star has an accretion disk in most young binary systems (see, e.g., Mathieu et al. 2000). The accretion disk is most likely to be replenished by accretion from a circumbinary disk. In fact, circumbinary disks are observed in some young binary systems as molecular rings (see, e.g., Roddier et al. 1996; Duvert et al. 1998; Close et al. 1998). If gas is accreted from the circumbinary disk to the circumstellar disk, the accretion rate will be nearly equal to the accretion rates of the primary and secondary stars in the long term. In other words, the accretion from the circumbinary disk controls the accretion of each component star.

The accretion in a protobinary system has been studied by Bate & Bonnell (1997) with hydrodynamic simulations. They assumed a binary system having a circular orbit and computed the accretion using a three-dimensional smoothed particle hydrodynamics (3DSPH) code. In their simulations the secondary accretes more gas than the primary when the accreting gas has a moderately large specific angular momentum. This result is also consistent with the earlier ballistic models (Artymowicz 1983; Bate 1997) and was explained by the fact that the secondary has a larger orbit than the primary. Artymowicz & Lubow (1996) obtained a similar conclusion for eccentric orbits.

If the secondary accretes more, the mass ratio increases and the system approaches being an equal-mass binary. Nevertheless,

the mass ratio distribution is flat in the range of $q \geq 0.2$ except for the detection bias (see, e.g., Woitas et al. 2001; White & Ghez 2001; Patience et al. 2002). There is no evidence that the secondary tends to have a larger accretion rate. In order to study this apparent contradiction, we have reexamined accreting protobinaries on the basis of two-dimensional hydrodynamic simulations with high resolution.

When the gas has a moderately large angular momentum, the gas flows into the binary system through L2, the Lagrange point close to the secondary. However, it does not flow directly into the secondary in our new computations. It flows halfway around the secondary from L2 to L1, where L1 denotes the Lagrange point between the primary and secondary. Then it flows around the primary and forms a circumstellar ring. Only a small amount of the gas flows back to the secondary through the L1 point. Consequently, the secondary has a less massive circumstellar ring. This difference comes mainly from the large numerical viscosity of earlier numerical simulations. We have confirmed that the secondary accretes more when the spatial resolution is low and hence the numerical viscosity is large.

This paper is organized as follows. Our model and numerical methods are given in § 2. Numerical results are shown in § 3. A part of the results are shown in the frame corotating with the binary. The corotation frame helps our understanding, since the flow is quasi-stationary and a particle has a constant of motion, the Jacobi integral. We discuss the dependence of the accretion rate on the specific angular momentum of the infalling gas in § 4. We also discuss implications of our numerical simulations on the distribution of the mass ratio in § 4. A brief summary is given in § 5.

2. MODEL AND METHOD OF COMPUTATION

We consider a pair of protostars that have been formed through collapse and fragmentation of a single molecular cloud core. They are still embedded in the molecular cloud and accrete gas from the infalling envelope. For simplicity we assume that

¹ Mathematical Sciences and Physics, Graduate School of Science and Technology, Chiba University, Inage-ku, Chiba 263-8522, Japan; yasuihiro@astro.s.chiba-u.ac.jp.

² Department of Astrophysics, School of Science, Nagoya University, Chikusa-ku, Nagoya 464-8602, Japan.

³ Center for Frontier Science, Chiba University, Inage-ku, Chiba 263-8522, Japan.

the protostars rotate around the center of the gravity with circular orbits. The infalling envelope is assumed to be coplanar with the orbits.

We approximate the accretion from the infalling envelope by the two-dimensional flow in the orbital plane. The accreting gas is assumed to be isothermal and to have constant sound speed, c_s . Then we solve the two-dimensional hydrodynamic equations,

$$\frac{\partial \Sigma}{\partial t} + \nabla \cdot (\Sigma \mathbf{v}) = 0, \quad (1)$$

and

$$\frac{\partial \mathbf{v}}{\partial t} + (\mathbf{v} \cdot \nabla) \mathbf{v} + c_s^2 \nabla \ln \Sigma + \nabla \Phi = 0, \quad (2)$$

where Σ , \mathbf{v} , and Φ denote the surface density of the gas, the gas velocity, and the gravitational potential, respectively.

The self-gravity of the accreting gas is ignored for simplicity. We also ignore the increase in the mass of stars through accretion for simplicity. Thus, the masses of the primary and secondary are set constant at M_1 and M_2 , respectively. The primary and secondary are assumed to rotate circularly with angular velocity

$$\omega = \sqrt{\frac{G(M_1 + M_2)}{a^3}}, \quad (3)$$

where G and a are the gravitational constant and the separation between the primary and secondary, respectively. The gravitational potential is evaluated to be

$$\Phi(r, t) = \sum_{i=1}^2 \Phi_i(r, t), \quad (4)$$

$$\Phi_i = \begin{cases} -\frac{GM_i}{|r - r_i|} & \text{for } |r - r_i| \geq R_i, \\ -\frac{GM_i}{2R_i^3} (3R_i^2 - |r - r_i|^2) & \text{otherwise,} \end{cases} \quad (5)$$

where r_i and R_i denote the position and the effective radius of each star, respectively. We set $R_1 = R_2 = 0.2a$ in most models. This artificial softening barely affects our results as long as the effective radii are appreciably smaller than the Roche lobe radius.

The hydrodynamic equations are solved on a Cartesian grid with a second-order-accurate finite-difference scheme. Our difference scheme is based on the total variation diminishing (TVD) scheme of Roe (1981). We achieved second-order accuracy using MUSCL (see, e.g., Hirsch 1990).

The Cartesian grid covers the square region of $-L \leq x, y \leq L$, and the value of L is taken to be $5.12a$ in most computations. The Cartesian grid contains 2048×2048 square cells in most models and 4096×4096 square cells in high-resolution models. The center of the grid coincides with the center of gravity.

At the initial stage ($t = 0$), the surface density is set to be

$$\Sigma = \begin{cases} 1 & \text{for } \sqrt{x^2 + y^2} > R_{\text{out}}, \\ 0.01 & \text{for } \sqrt{x^2 + y^2} \leq R_{\text{out}}, \end{cases} \quad (6)$$

where R_{out} denotes the radius of the effective outer boundary and is set to be $R_{\text{out}} = 5.10a$ in most models. The initial velocity is set to be

$$\mathbf{v}_0 = \frac{j_{\text{inf}}}{R_{\text{out}}^2} \begin{pmatrix} -y \\ x \end{pmatrix} - \frac{v_{\text{inf}}}{\sqrt{x^2 + y^2}} \begin{pmatrix} x \\ y \end{pmatrix}, \quad (7)$$

$$v_{\text{inf}} = \sqrt{\frac{2GM}{R_{\text{out}}} - \frac{j_{\text{inf}}^2}{R_{\text{out}}^2}}, \quad (8)$$

where v_{inf} and j_{inf} are model parameters specifying the radial infall velocity and the specific angular momentum of the infalling gas, respectively. We regard j_{inf} as the model parameter. The radial infall velocity is set so that the total specific energy,

$$E \simeq \frac{1}{2} \left(v_{\text{inf}}^2 + \frac{j_{\text{inf}}^2}{R_{\text{out}}^2} \right) - \frac{GM}{R_{\text{out}}} = 0, \quad (9)$$

vanishes. Equation (9) means that the gas is accreted very far from the binary. The surface density and velocity are kept at the initial values in the region of $r \equiv (x^2 + y^2)^{1/2} \geq R_{\text{out}}$. Thus, we have a constant inflow from the boundary of $r = R_{\text{out}}$ at the rate of $\dot{M}_{\text{inf}} = 2\pi R_{\text{out}} v_{\text{inf}}$.

We show our numerical simulations in the same nondimensional units as those in Bate & Bonnell (1997). Namely, the unit length is the separation (a) and the unit frequency is the angular velocity (ω). In most models we compute the flow for 15 rotation periods, i.e., from $t = 0$ to 30π .

3. RESULTS

We show our results in the following order. Model 6-16 ($q = 0.6$, $j_{\text{inf}} = 1.6$, and $c_s = 0.25$) is shown as a typical example in § 3.1. The dependence of accretion on j_{inf} is described in § 3.2. The dependence on q is shown in § 3.3. The dependence on c_s is shown in § 3.4. We focus our attention on sporadic variation in the accretion rate in § 3.5. Table 1 summarizes the average accretion rates of the primary and secondary, as well as their accretion rate ratios, for all the models we have computed.

3.1. Typical Model

As a typical example we describe model 6-16 in this subsection. The model parameters are set to be $q = 0.6$, $j_{\text{inf}} = 1.6$, and $c_s = 0.25$. We followed accretion onto the binary from $t = 0$ to 40π , as shown in Figure 1.

Figure 1a denotes the central region around the binary at the initial stage ($t = 0$). The surface density is quite low ($\log \Sigma = -2.0$) in all the regions shown in the figure. The curves denote the contours of the Roche potential.

The accreting gas forms a thin circumbinary ring at $t = 2.0\pi$ as shown in Figure 1b. The radial velocity is close to zero in the ring. The accreting gas is decelerated by the centrifugal force and forms a shock wave. The circumbinary ring consists of the post-shocked gas. If we approximate the gravity by the point mass gravity, $-GM/r$, the infall velocity should vanish at

$$r_c = \frac{j_{\text{inf}}^2}{2} a. \quad (10)$$

Substituting $j_{\text{inf}} = 1.6$, we obtain $r_c = 1.28$. This rough estimate is consistent with the radius of the circumbinary ring.

TABLE 1
 MODEL PARAMETERS AND AVERAGE ACCRETION RATES OF THE PRIMARY AND SECONDARY OVER THE PERIOD $20\pi \leq t \leq 30\pi$

Model	q	j_{inf}	c_s	Cells	L	\dot{M}_{1d}	\dot{M}_{2d}	$\dot{M}_{1d}/\dot{M}_{2d}$
2-12	0.2	1.2	0.25	6144 ²	5.12a	4.84	4.12	1.17
2-13	0.2	1.3	0.25	6144 ²	5.12a	4.78	2.57	1.86
3-12	0.3	1.2	0.25	6144 ²	5.12a	5.18	3.39	1.53
3-13	0.3	1.3	0.25	6144 ²	5.12a	4.55	2.05	2.22
4-13	0.4	1.3	0.25	2048 ²	5.12a	3.98	4.58	0.871
4-14	0.4	1.4	0.25	2048 ²	5.12a	3.74	4.66	0.803
4-15	0.4	1.5	0.25	2048 ²	5.12a	2.51	1.29	1.94
4-16L	0.4	1.6	0.20	2048 ²	5.12a	3.36	1.34	2.51
4-16	0.4	1.6	0.25	4096 ²	5.12a	1.88	0.774	2.44
4-16H	0.4	1.6	0.30	2048 ²	6.63a	1.43	0.424	3.37
4-17	0.4	1.7	0.25	2048 ²	5.12a	2.11	0.701	3.01
4-18	0.4	1.8	0.25	2048 ²	5.12a	0.625	0.279	2.24
4-19	0.4	1.9	0.25	2048 ²	5.12a	0.241	0.129	1.87
5-13	0.5	1.3	0.25	2048 ²	5.12a	5.17	2.59	2.00
5-14	0.5	1.4	0.25	2048 ²	5.12a	4.39	2.43	1.81
5-15	0.5	1.5	0.25	2048 ²	5.12a	3.41	1.82	1.87
5-16	0.5	1.6	0.25	2048 ²	5.12a	2.44	0.982	2.49
5-17	0.5	1.7	0.25	2048 ²	5.12a	1.89	0.656	2.88
5-18	0.5	1.8	0.25	2048 ²	5.12a	0.729	0.295	2.68
5-19	0.5	1.9	0.25	2048 ²	5.12a	0.394	0.155	2.54
6-13	0.6	1.3	0.25	4096 ²	5.12a	5.20	2.59	2.01
6-14	0.6	1.4	0.25	2048 ²	5.12a	5.99	2.98	2.01
6-15	0.6	1.5	0.25	2048 ²	5.12a	3.31	1.84	1.80
6-16L	0.6	1.6	0.20	4096 ²	5.12a	2.84	1.46	1.94
6-16	0.6	1.6	0.25	4096 ²	5.12a	2.24	1.21	1.85
6-16a	0.6	1.6	0.25	6144 ²	5.12a	2.51	2.98	0.841
6-16b	0.6	1.6	0.25	8192 ²	5.12a	2.38	1.95	1.22
6-16c	0.6	1.6	0.25	2048 ²	5.12a	1.46	0.803	1.81
6-16H	0.6	1.6	0.30	4128 ²	6.60a	2.17	1.23	1.77
6-17	0.6	1.7	0.25	2048 ²	5.12a	2.00	0.733	2.73
6-18	0.6	1.8	0.25	2048 ²	5.12a	0.825	0.305	2.71
6-19LL	0.6	1.9	0.18	4096 ²	5.12a	0.778	0.432	1.80
6-19L	0.6	1.9	0.20	4096 ²	5.12a	0.594	0.144	4.11
6-19ML	0.6	1.9	0.23	2048 ²	5.12a	0.491	0.238	2.07
6-19	0.6	1.9	0.25	4096 ²	5.12a	0.577	0.200	2.88
6-19MH	0.6	1.9	0.27	2048 ²	5.12a	0.452	0.810	5.59
6-19H	0.6	1.9	0.30	4096 ²	6.63a	0.317	0.130	2.44
7-14	0.7	1.4	0.25	2048 ²	5.12a	6.19	3.65	1.69
7-15	0.7	1.5	0.25	2048 ²	5.12a	4.23	1.75	2.42
7-16	0.7	1.6	0.25	2048 ²	5.12a	2.05	0.407	5.03
7-17	0.7	1.7	0.25	2048 ²	5.12a	1.00	0.359	2.80
7-18	0.7	1.8	0.25	2048 ²	5.12a	1.05	0.307	3.41
7-19	0.7	1.9	0.25	2048 ²	5.12a	0.571	0.244	2.34
8-15	0.8	1.5	0.25	2048 ²	5.12a	3.10	0.942	3.29
8-16	0.8	1.6	0.25	2048 ²	5.12a	2.30	0.717	3.20
8-17	0.8	1.7	0.25	2048 ²	5.12a	0.796	0.267	2.98
8-18	0.8	1.8	0.25	2048 ²	5.12a	0.793	0.284	2.79
8-19	0.8	1.9	0.25	2048 ²	5.12a	0.495	0.271	1.83
9-15	0.9	1.5	0.25	2048 ²	5.12a	3.07	3.10	0.992
9-16	0.9	1.6	0.25	2048 ²	5.12a	2.88	1.94	1.49
9-17	0.9	1.7	0.25	2048 ²	5.12a	0.711	0.700	1.02
9-18	0.9	1.8	0.25	2048 ²	5.12a	0.723	0.352	2.05
9-19	0.9	1.9	0.25	2048 ²	5.12a	0.403	0.313	1.29
10-15	1.0	1.5	0.25	2048 ²	5.12a	2.09	1.39	1.51
10-16	1.0	1.6	0.25	2048 ²	5.12a	1.02	1.02	0.994
10-17	1.0	1.7	0.25	2048 ²	5.12a	0.587	0.311	1.89
10-18	1.0	1.8	0.25	2048 ²	5.12a	0.693	0.652	1.06
10-19	1.0	1.9	0.25	2048 ²	5.12a	0.396	0.432	0.915

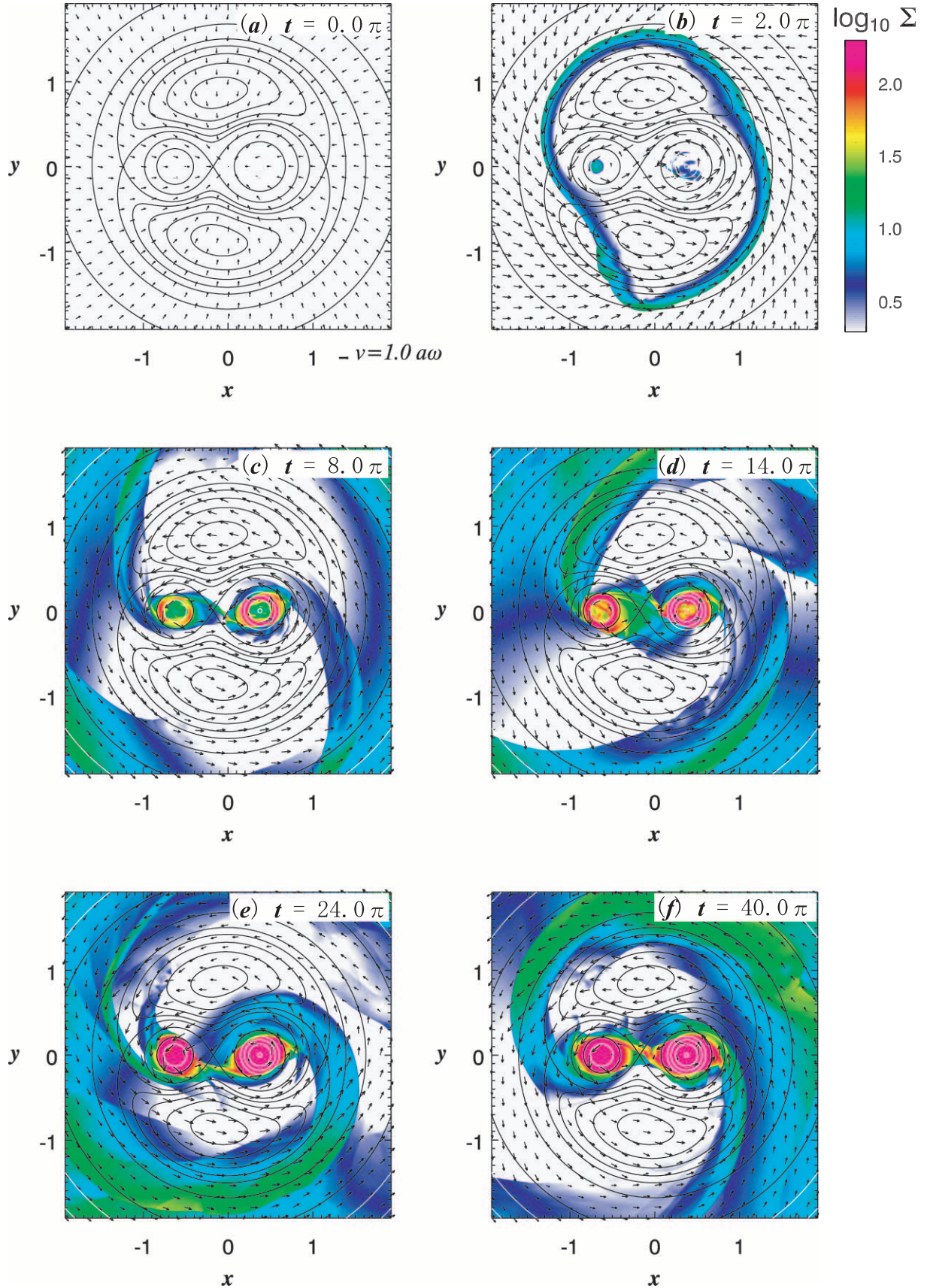


FIG. 1.—Time evolution of gas accretion for model 6-16. Each panel denotes the surface density distribution by color and the velocity distribution by arrows. The color scale is shown in the right of (b). The velocity scale is shown below (a). The curves are the contours of the Roche potential. These panels denote the stages of $t = 0, 2.0\pi, 8.0\pi, 14.0\pi, 24.0\pi$, and 40.0π . The primary and secondary are located at $(x, y) = (0.375, 0.0)$ and $(-0.625, 0.0)$, respectively, at all the stages shown above.

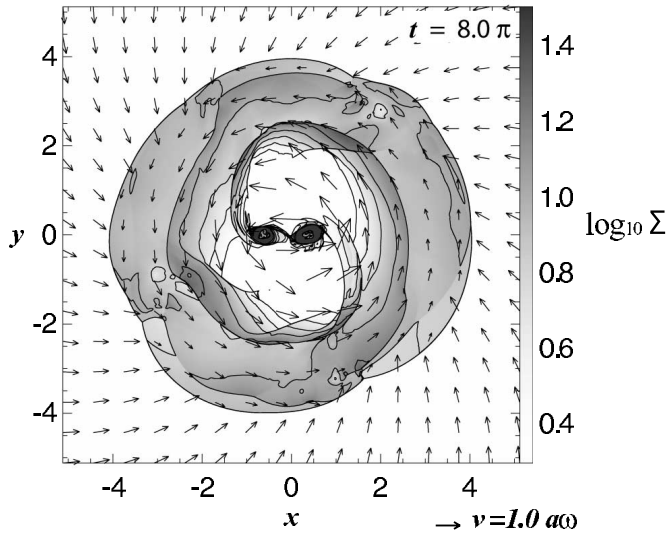


FIG. 2.—Entire region of computation for the stage of $t = 8.0\pi$ for model 6-16. The same stage is shown in Fig. 1c. The gray scale and contours denote the surface density. The circumbinary ring has inner and outer radii of $r \simeq 1.5$ and 4, respectively. It has two spiral arms that stem from the L2 and L3 points.

Note that the circumbinary ring passes L2, i.e., the Lagrange point close to the secondary.

Figure 1c shows the stage of $t = 8.0\pi$. The circumbinary ring has two spiral arms, and one of them reaches the L2 point. The binary accretes gas mainly through the L2 point. Note that not only the secondary but also the primary has a circumstellar ring. The circumprimary ring is more massive than the circumsecondary ring.

Figures 1d, 1e, and 1f show the stages of $t = 14.0\pi$, 24.0π , and 40.0π , respectively. Both the circumprimary and circumsecondary disks grow in mass. The gas is supplied mainly through the L2 point and partly through the L3 point. In the following we call the gas stream through the L3 point channel A and that through L2 channel B. The mass supply through channel B is continuous, while that through channel A is intermittent. One of the spiral arms reaches the L2 point persistently, while the other reaches the L3 point only occasionally. The surface density is very low near the L4 and L5 points. These low surface density regions shrink in area as the time passes. Although the circumprimary and circumsecondary disks accrete onto the primary and secondary, the accretion is due to numerical viscosity. The circumprimary and circumsecondary disks are supported against the gravity mainly by the centrifugal force. The gas pressure is much smaller than the gravity since the sound speed is low.

Figure 2 shows the surface density distribution at $t = 8.0\pi$ for the whole computation box. The circumbinary disk has an outer radius of $r \simeq 4$ and an inner radius of $r \simeq 1.5$. The spiral arms wind roughly 2π from the L2 and L3 points to the outer edge of the circumbinary disk. The outer edge extends with the time. The gas is accumulated in the circumbinary disk.

The spiral arms corotate with the binary as shown in Figure 1. Thus, these arms are waves similar to those seen in spiral galaxies. To examine the dynamics of the spiral waves we denote the velocity measured in the corotation frame in Figure 3 for the stage of $t = 14.0\pi$ which is also shown in Figure 1d. The gas flow is not along the spiral arms. The gas circulates counterclockwise inside the Roche lobe, while it goes clockwise outside the Roche lobe. The gas is decelerated on the spiral arms and accretes into the Roche lobe through the L2 point and occasionally also through the L3 point.

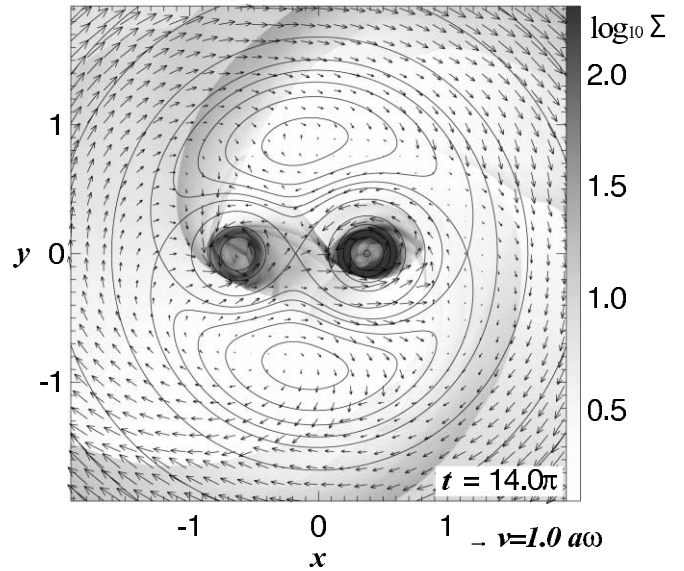


FIG. 3.—Same as Fig. 1d but for the velocity. The arrows denote the velocity measured in the corotation frame. When measured in the corotation frame, the gas rotates clockwise outside the Roche lobe.

Figure 4 shows the streamlines (*thin solid lines*) around the secondary and the surface density distribution (*gray scale*) at $t = 6.0\pi$. The thick solid circle denotes the effective radius of the secondary. The streamlines are constructed from the velocity field measured in the corotation frame. There are two stagnation points: one near the L1 point and the other near the L2 point. The flow bifurcates from the circumbinary disk near the L2 point and flows into the Roche lobe. After circulating halfway around the secondary, it enters into the primary lobe and circulates around the primary. The flow around the primary as well as that around the secondary is counterclockwise in the corotation frame. The flow from the secondary lobe collides with that from the primary lobe near the L1 point. After the collision, only a minor fraction of the gas flows toward the secondary.

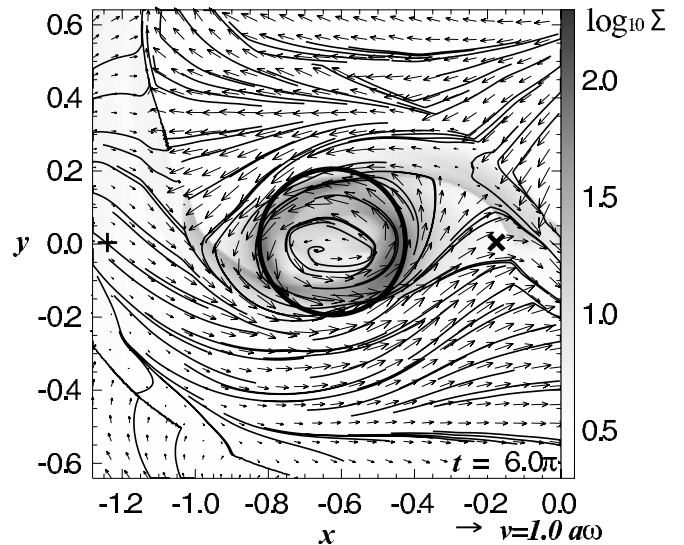


FIG. 4.—Streamlines (*solid lines*) are overlaid on the surface density distribution (*gray scale*) at $t = 6.0\pi$ in model 6-16. The thick circle denotes the effective radius of the secondary. The plus sign and cross denote the L2 and L1 points, respectively.

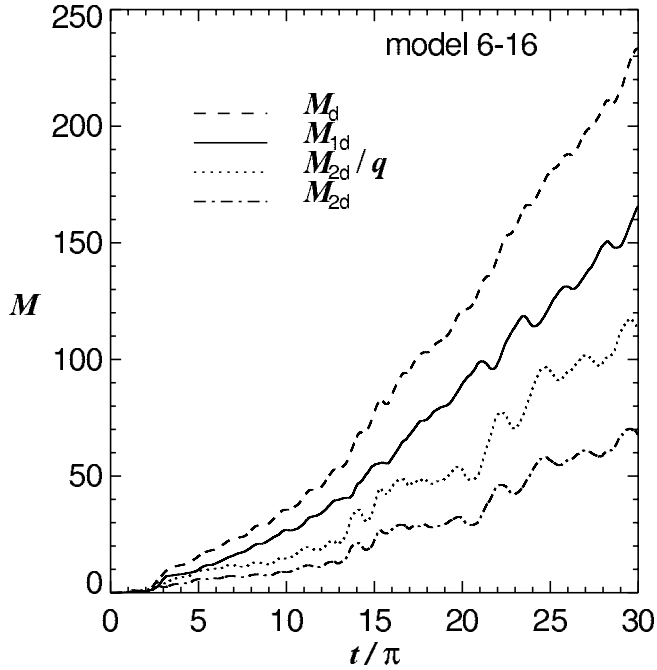


FIG. 5.—Time evolution of the circumstellar disk masses in model 6-16. The ordinates denote the time in units of π . The solid curve denotes the disk mass for the primary (M_{1d}) and the dash-dotted curve does that for the secondary (M_{2d}). The dashed curve denotes the total of the primary and secondary disk masses ($M_d \equiv M_{1d} + M_{2d}$). The dotted curve denotes M_{2d}/q for evaluating the change in the mass ratio by comparing with M_{1d} .

Note that the gas streaming into the Roche lobe does not intersect the spiral shock. Since the flow is nearly stationary in the corotation frame, the Bernoulli constant,

$$\varepsilon = \frac{|\mathbf{v}'|^2}{2} + \Phi - \frac{\omega^2 |r|^2}{2} + c_s^2 \ln \Sigma, \quad (11)$$

should be constant along the streamline. The last term in equation (11) denotes the Gibbs free energy. We have confirmed that ε is constant along the streamline connecting the L2 and L1 points. This implies that the numerical energy dissipation is negligibly small.

To measure the accretion we evaluate the circumprimary disk mass, M_{1d} , from the gas contained within a circle having the primary at the center for simplicity. The radius of the circle is taken to be the distance between the L1 point and the center of the primary. This circle is somewhat larger than the circumprimary disk, and hence our disk mass is a little overestimated. A part of the gas contained in the circle is not gravitationally bound to the primary. Similarly, we evaluate the circumsecondary disk mass, M_{2d} .

Figure 5 denotes M_{1d} (solid curve) and M_{2d} (dash-dotted curve) as a function of time. Both M_{1d} and M_{2d} increase with time while oscillating appreciably. The oscillation is in part due to our definition of M_{1d} and M_{2d} . An appreciable amount of the gas crosses the circles, and the disk masses increase (or decrease) temporarily. The average accretion rate is larger for the primary than for the secondary, $\dot{M}_{1d} > \dot{M}_{2d}$. It is $\dot{M}_{1d} = 1.014$ and $\dot{M}_{2d} = 0.305$ over the period $2.0\pi \leq t \leq 12.0\pi$. These numbers are obtained from the least-squares fit to M_{1d} and M_{2d} . The change in the mass ratio is computed to be

$$\dot{q} = -\frac{q}{M_{1d}} \left(\dot{M}_{1d} - \frac{\dot{M}_{2d}}{q} \right). \quad (12)$$

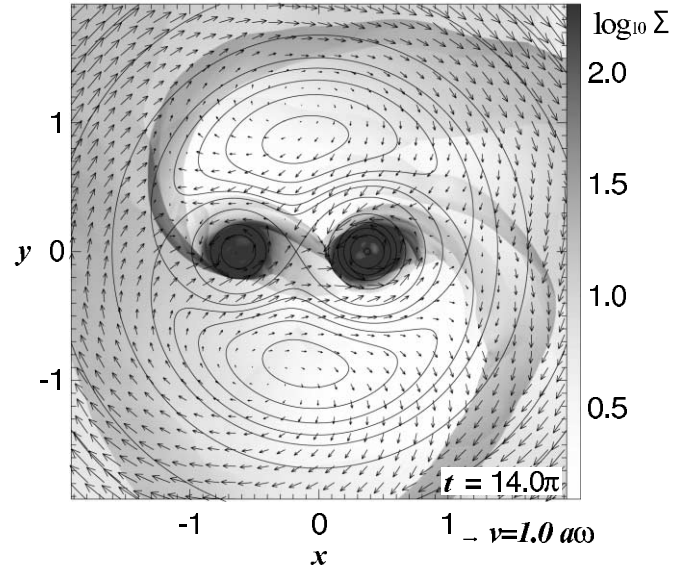


FIG. 6.—Same as Fig. 3 but for model 6-13.

This accretion decreases the mass ratio, since $\dot{M}_{1d} > \dot{M}_{2d}/q$. We denote \dot{M}_{2d}/q by the dotted curve in Figure 5 to easily assess the change in the mass ratio.

The accretion rate increases appreciably around $t \simeq 14\pi$. The average accretion rate is $\dot{M}_{1d} = 2.24$ for the primary and $\dot{M}_{2d} = 1.21$ for the secondary over the period $20.0\pi \leq t \leq 30.0\pi$. The mass ratio also decreases in this period.

The mass accretion from the outer boundary is $\dot{M}_{\text{inf}} = 17.4$ in model 6-16. Since it is much larger than \dot{M}_{1d} and \dot{M}_{2d} , the gas inflow from the boundary remains mainly in the circumbinary disk.

3.2. Dependence on j_{inf}

We show models 6-13, 6-14, 6-15, 6-17, 6-18, and 6-19 in this subsection to examine the dependence on the specific angular

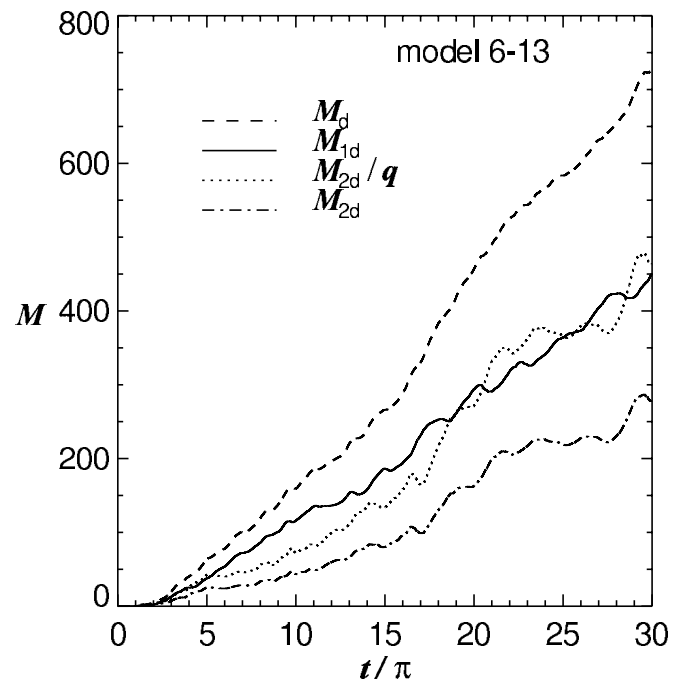


FIG. 7.—Same as Fig. 5 but for model 6-13.

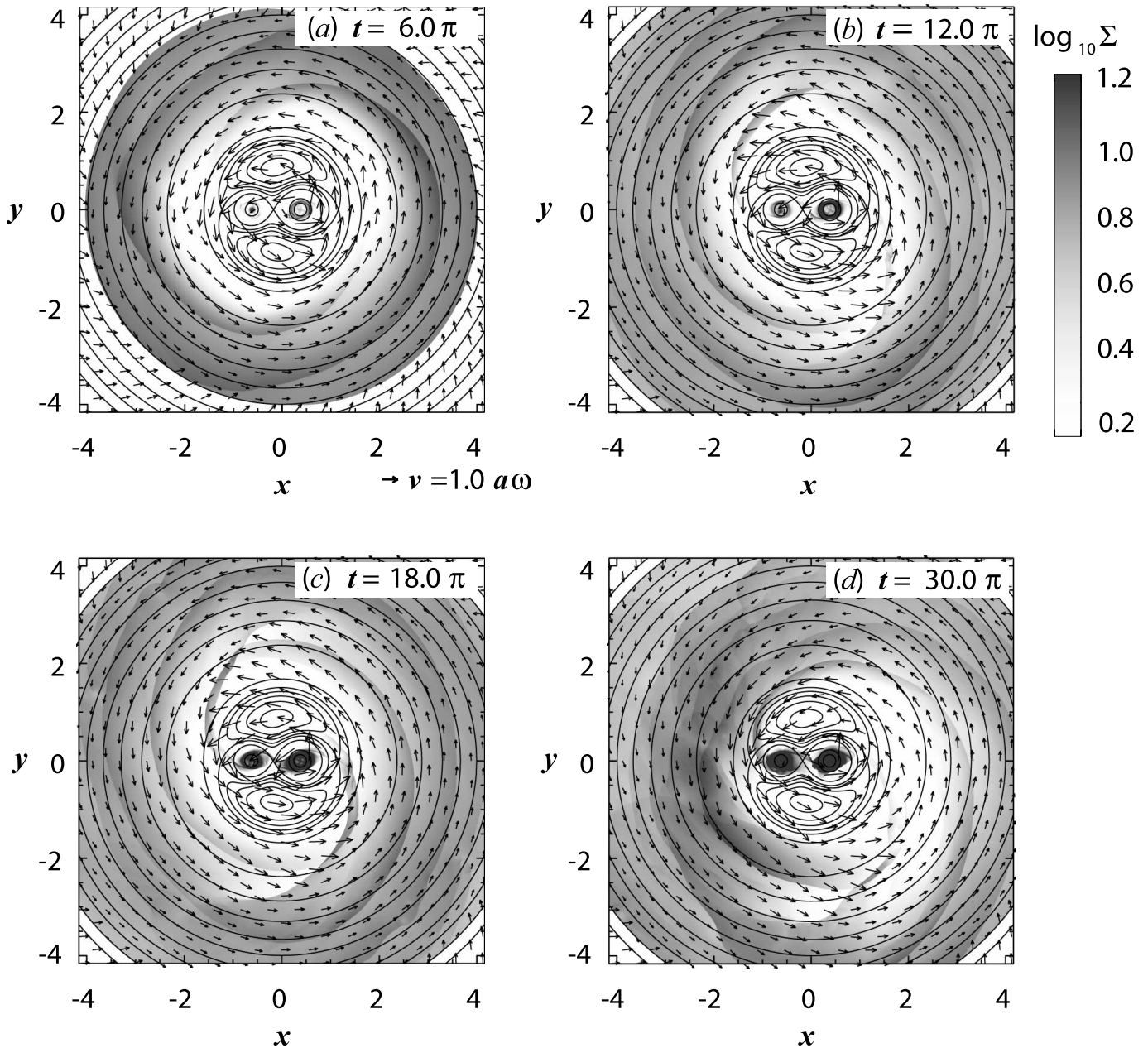


FIG. 8.—Time evolution of gas accretion in model 6-19. Each panel denotes the surface density and velocity measured in the rest frame by gray scale and arrows, respectively, at a given stage. The curves are the contours of the Roche potential.

momentum of infalling gas, j_{inf} . All these models have the same model parameters, $q = 0.6$ and $c_s = 0.25$. Only the specific angular momentum of the accreting gas, j_{inf} , is different. Each model number denotes $10q$ and $10j_{\text{inf}}$. These models are classified into three groups: models having a small j_{inf} (6-13 and 6-14), those having a medium j_{inf} (6-15, 6-16, and 6-17), and those having a large j_{inf} (6-18 and 6-19).

First we show model 6-13, in which the infalling gas has $j_{\text{inf}} = 1.3$. The infalling gas forms a circumbinary ring at $t \simeq 2.0\pi$ as in model 6-16. However, the ring radius is smaller than in model 6-16, since j_{inf} is smaller (see eq. [10]).

Figure 6 shows the surface density distribution at $t = 14.0\pi$ for model 6-13. The arrows denote the velocity measured in the corotation frame. The binary accretes gas appreciably not only through channel B but also through channel A. The two spiral arms have comparable surface densities. They are less wound in

model 6-13 than in model 6-16. The circumpriary and circumssecondary disks are more massive in model 6-13 than in model 6-16.

Figure 7 shows the masses of the circumpriary and circumssecondary disks as a function of time. The accretion rate is nearly constant in model 6-13, while it increases appreciably in model 6-16 (see Fig. 5). The average accretion rate is $\dot{M}_{1d} = 5.18$ for the primary and $\dot{M}_{2d} = 3.34$ for the secondary over the period $2.0\pi \leq t \leq 30.0\pi$. This accretion decreases the mass ratio a little, since \dot{M}_{1d} is only slightly larger than \dot{M}_{2d}/q .

Model 6-14 is qualitatively similar to model 6-13. The accretion through channel A is steady in both models 6-13 and 6-14.

Next we show models 6-18 and 6-19, both of which have a large j_{inf} . Figure 8a shows the surface density distribution at $t = 6.0\pi$ in model 6-19 ($j_{\text{inf}} = 1.9$). Gas accretes little during

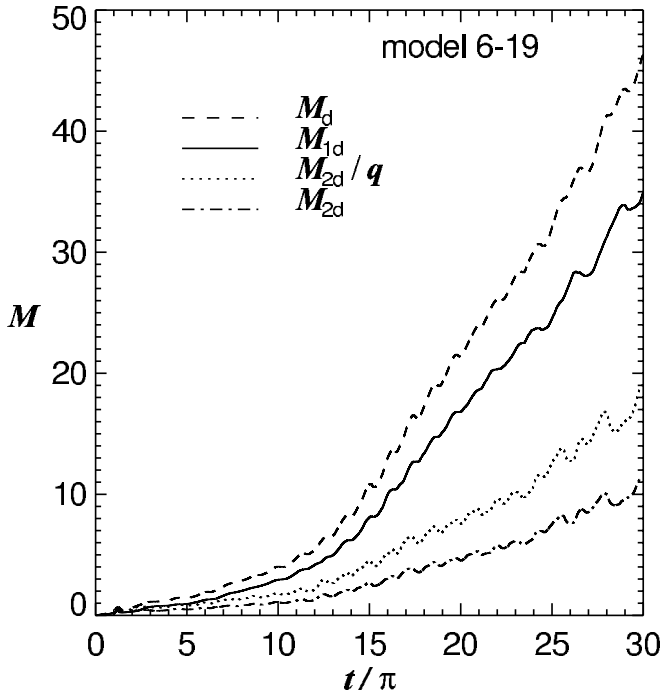


FIG. 9.—Same as Fig. 5 but for model 6-19.

the first several rotations in models of $j_{\text{inf}} \geq 1.8$. The circumbinary disk's inner edge is at $r \simeq 2.1$ at this stage. The gas in the circumbinary disk still has a large specific angular momentum and does not yet accrete on either the primary or the secondary. The circumstellar rings at this stage consist of low surface density gas filled in $r < R_{\text{out}}$ at the initial stage. The initial low surface density gas has a low specific angular momentum and thus accretes on a dynamical timescale. The circumprimary and circumsecondary disks have $M_{1d} = 1.23$ and $M_{2d} = 0.647$, respectively, at $t = 6.0\pi$.

Figure 8b is the same as Figure 8a but for the stage at $t = 12.0\pi$. The circumbinary disk has a spiral arm extending toward the L2 point. The tip of the spiral arm is, however, still detached from the circumsecondary disk. Figures 8c and 8d show the stages at $t = 18.0\pi$ and 30.0π , respectively. The circumbinary disk has two spiral arms, one of which is connected with the circumsecondary disk near the L2 point and the other of which extends toward the L3 point. The binary accretes gas through the L2 point at these stages.

Figure 9 shows M_{1d} and M_{2d} as a function of time. The accretion rate increases by a factor of 4.89 for the primary and 4.37 for the secondary around $t \simeq 13\pi$. The average accretion rate of the primary is $\dot{M}_{1d} = 7.01 \times 10^{-2}$ in $0 \leq t \leq 4\pi$ and 5.59×10^{-1} in $16\pi \leq t \leq 30\pi$. That of the secondary is $\dot{M}_{2d} = 4.07 \times 10^{-2}$ in $0 \leq t \leq 4\pi$ and 1.73×10^{-1} in $16\pi \leq t \leq 30\pi$. The accretion rate is fairly constant in $16\pi \leq t \leq 30\pi$. The ratio of the accretion rates is $\dot{M}_{1d}/\dot{M}_{2d} = 3.22$. Again the primary accretes more and the accretion decreases the mass ratio, q .

Model 6-18 is qualitatively similar to model 6-19. Also in model 6-18, the accretion rate is small in $0 \leq t \leq 12\pi$. The duration of the early very low accretion rate phase is longer for a larger j_{inf} . When j_{inf} is larger, it takes more time for gas to lose its angular momentum. The early very low accretion rate phase does not exist when $j_{\text{inf}} \leq 1.7$.

Models 6-15 and 6-17 are qualitatively similar to model 6-16. The gas accretes onto the binary mainly through channel B, i.e.,

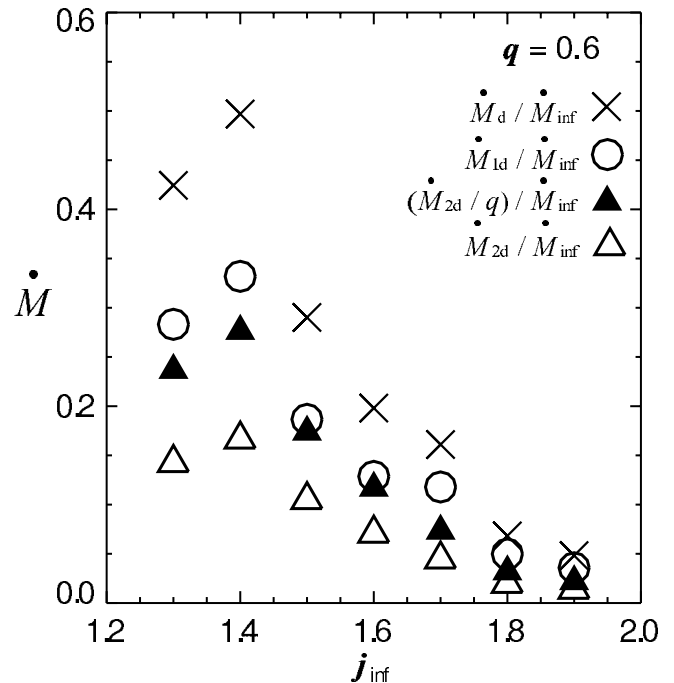


FIG. 10.—Accretion rate as a function of the specific angular momentum of the accreting gas, j_{inf} . The mass ratio and the sound speed are fixed at $q = 0.6$ and $c_s = 0.25$. The accretion rate is measured over the period $20\pi \leq t \leq 30\pi$, during which it is nearly constant in a model. It is normalized by the accretion rate from the outer boundary, \dot{M}_{inf} . The open circles denote the accretion rate of the primary, \dot{M}_{1d} , and the open triangles denote that of the secondary, \dot{M}_{2d} . The crosses denote the sum of them, \dot{M}_d , and the filled triangles denote \dot{M}_{2d}/q .

through the L2 point in these models. The accretion sets in around $t \simeq 2\pi$.

As shown above, models of $q = 0.6$ are classified into three groups according to j_{inf} . When $j_{\text{inf}} \lesssim 1.45$, the gas accretes onto the binary through both channels A and B. We call such accretion type I. When $j_{\text{inf}} \gtrsim 1.75$, the gas accretion is little in the first several rotations. The gas accretion begins after a spiral arm extending from the circumbinary disk reaches the L2 point. It is only through channel B. We call such accretion type III. When j_{inf} is intermediate ($1.45 \lesssim j_{\text{inf}} \lesssim 1.75$), the gas accretes mainly through channel B. We call such accretion type II.

Figure 10 shows the average accretion rate in $20\pi \leq t \leq 30\pi$ as a function of j_{inf} . The crosses denote the ratio of total accretion rate of the binary to the accretion rate from the outer boundary, $\dot{M}_d/\dot{M}_{\text{inf}}$. The total accretion rate is lower for a larger j_{inf} in general, although it does not decrease monotonically with increasing j_{inf} . The open circles and open triangles denote $\dot{M}_{1d}/\dot{M}_{\text{inf}}$ and $\dot{M}_{2d}/\dot{M}_{\text{inf}}$, respectively. The accretion rate of the primary is larger than that of the secondary in all the models shown in the diagram. The filled triangles denote $\dot{M}_{2d}/(q\dot{M}_{\text{inf}})$ to evaluate the change in the mass ratio from comparison with $\dot{M}_{1d}/\dot{M}_{\text{inf}}$. The latter is slightly larger than the former, and thus the mass ratio decreases in all the models.

3.3. Dependence on the Mass Ratio q

In this subsection we examine dependence on the mass ratio, q , by comparing models having various q and j_{inf} .

Figure 11 shows the surface density distribution at $t = 24.0\pi$ for models 4-16, 7-16, and 9-16. These models, as well as model 6-16, have the same $j_{\text{inf}} = 1.6$ but different q . All these models are qualitatively similar; they show type II accretion, and the primary accretes more gas than the secondary.

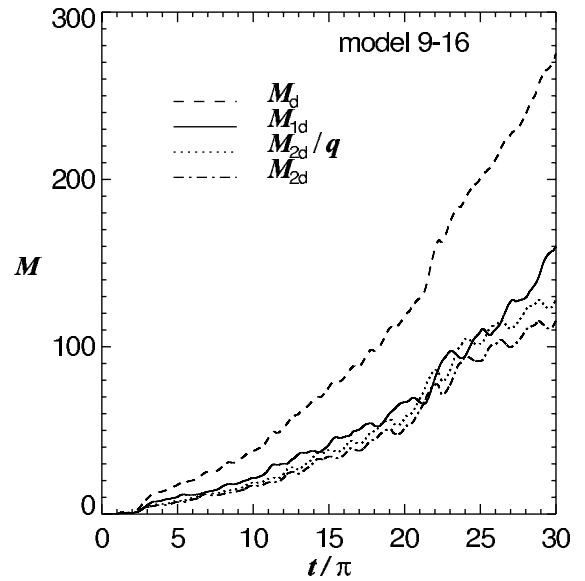
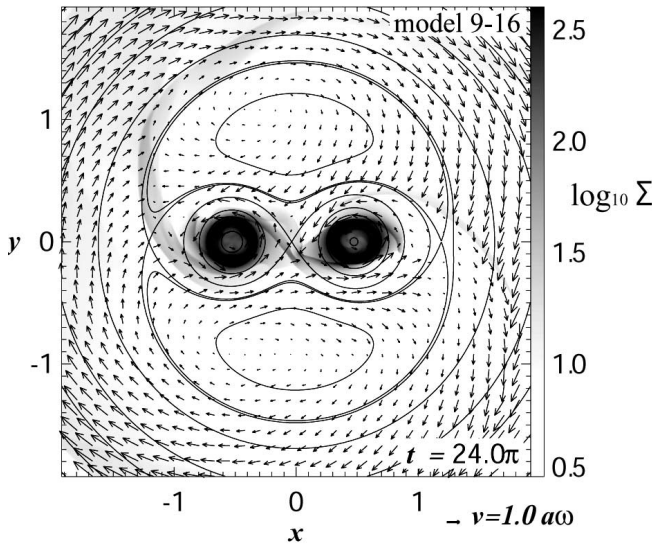
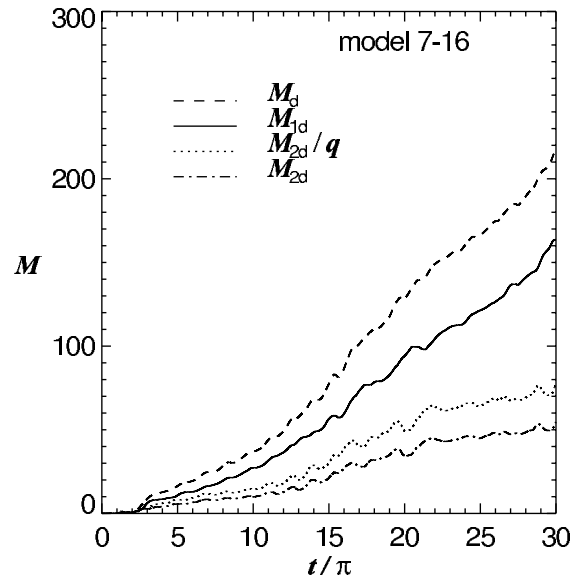
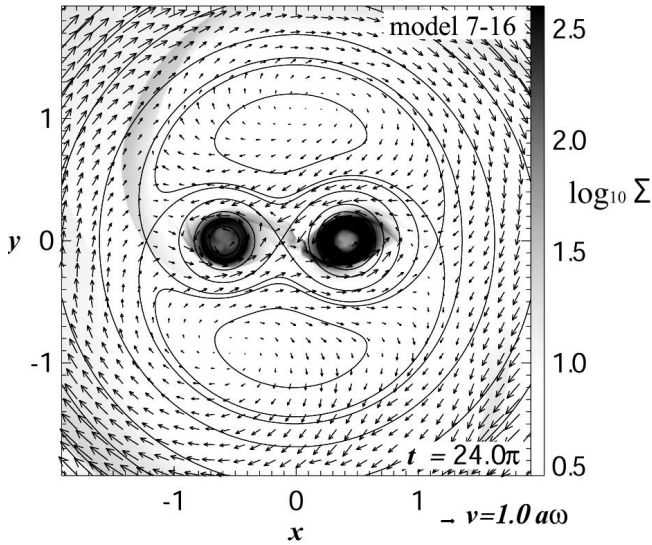
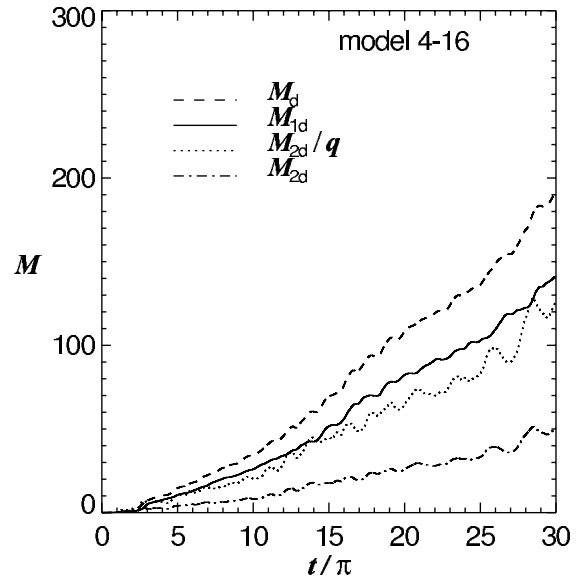
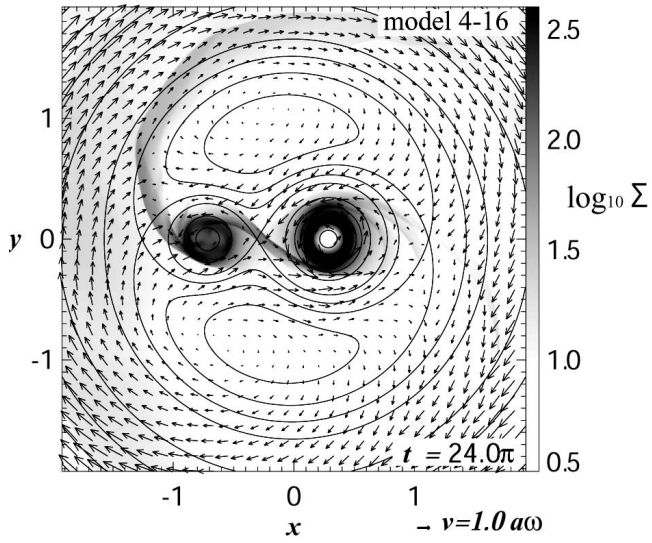


FIG. 11.—Surface density distributions at $t = 24.0\pi$ for models 4-16, 7-16, and 9-16. These models have the same model parameters except for the mass ratio, q . The arrows denote the velocity measured in the corotation frame. The curves denote the contours of the Roche potential.

FIG. 12.—Same as Fig. 5 but for models 4-16, 7-16, and 9-16, respectively.

TABLE 2
THE AVERAGE ACCRETION RATES OF THE PRIMARY AND SECONDARY

MODEL	PRIMARY			SECONDARY			\dot{M}_{inf}
	t_{break}	$\dot{M}_{1d,\text{early}}$	$\dot{M}_{1d,\text{late}}$	t_{break}	$\dot{M}_{2d,\text{early}}$	$\dot{M}_{2d,\text{late}}$	
4-16	13.00π	1.058	2.100	10.83π	0.307	0.802	17.40
7-16	15.44π	1.177	2.058	13.26π	0.350	0.633	17.39
9-16	20.20π	1.041	2.787	20.19π	0.884	1.940	17.39

Figure 12 shows the time evolution of the circumstellar disk masses for models 4-16, 7-16, and 9-16. The circumprimary disk is more massive than the circumsecondary disk in all the models. The accretion rate increases twice in all the models.

See Table 2 for the average accretion rates in the early phase ($\dot{M}_{1d,\text{early}}$ and $\dot{M}_{2d,\text{early}}$) and those in the late phase ($\dot{M}_{1d,\text{late}}$ and $\dot{M}_{2d,\text{late}}$). These values are obtained by the piecewise best linear fit to M_{1d} and M_{2d} . The epoch of the increase in the accretion rate (t_{break}) is evaluated from the crossing of the two piecewise best fits. As shown in Table 2, the epoch (t_{break}) is later for a larger q both for the primary and for the secondary.

We find, however, quantitative differences between these models. The mass ratio decreases in models 4-16 and 7-16, since $M_{1d} \gtrsim M_{2d}/q$. The mass ratio changes only a little in model 9-16 since $M_{1d} \simeq M_{2d}/q$.

Figure 13 shows the accretion rate of the primary, \dot{M}_{1d} , as a function of q and j_{inf} . The height of each bar denotes the accretion rate for given j_{inf} and q . It is shown in units of the accretion rate from the outer boundary. The left panel shows the accretion rate in the early phase, $2\pi \leq t \leq 12\pi$, while the right panel shows that in the late phase, $20\pi \leq t \leq 30\pi$. Both in the early and late phases, the accretion rate is higher for a smaller j_{inf} but depends a little on q . The accretion rate is higher in the late phase than in the early phase. The increase in the accretion rate is prominent when j_{inf} is large.

The left panel of Figure 14 shows the ratio of the accretion rates, $\dot{M}_{1d}/\dot{M}_{2d}$, for various j_{inf} and q . The ratio is evaluated from the average accretion rates in the late phase. It ranges from 0.80 to 5.03 and is larger than unity in most models. In other words, the primary accretes more in most models.

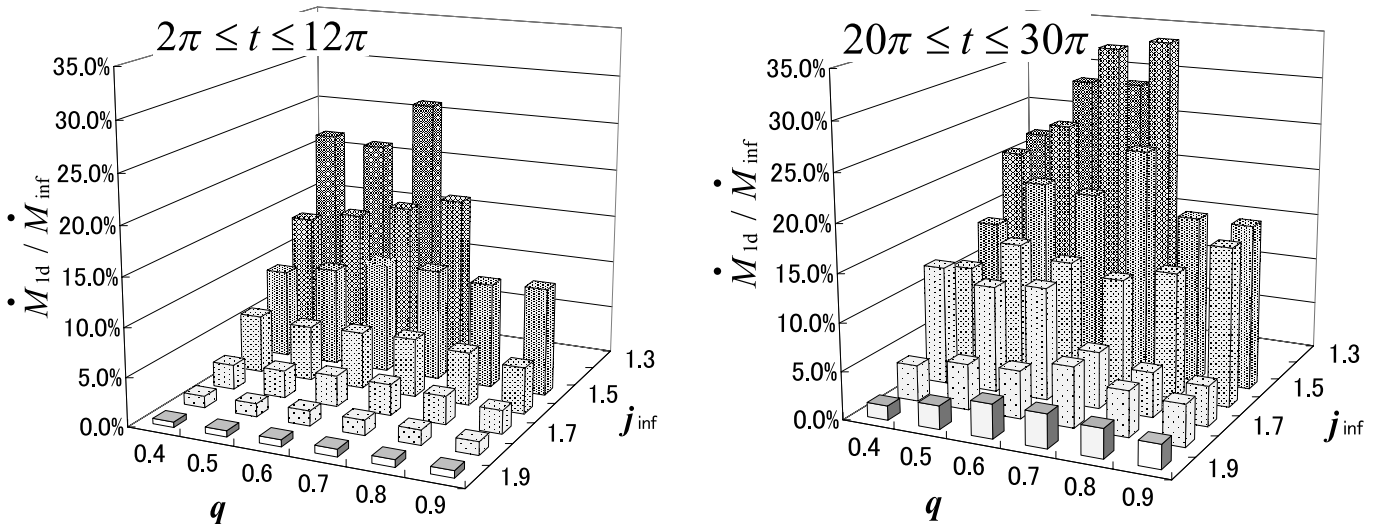


FIG. 13.—Dependence of accretion rate of the primary on the mass ratio q and specific angular momentum of the accreting gas, j_{inf} . The accretion rate is the average over the period $2\pi \leq t \leq 12\pi$ (left) and $20\pi \leq t \leq 30\pi$ (right). Accretion rate of the primary is normalized by the accretion rate from the outer boundary, \dot{M}_{inf} . The gray scale denotes j_{inf} .

The right panel of Figure 14 is essentially the same as the left panel but shows $q\dot{M}_{1d}/\dot{M}_{2d} - 1$. It is proportional to the change in the mass ratio, $-\dot{q}$. The bars with black tops denote models having a positive \dot{q} . The mass ratio decreases in the other models.

Note that Figures 13 and 14 show both systematic and sporadic variations in the accretion rate as a function of q and j_{inf} . We discuss the origin of the sporadic variation in § 3.5.

The total accretion rate, $\dot{M}_{1d} + \dot{M}_{2d}$, is less than $0.545\dot{M}_{\text{inf}}$ in all the models. The majority of the gas is accumulated in the circumbinary disk.

Figure 15 summarizes the type of accretion in the $q - j_{\text{inf}}$ plane. The double circles denote the models in which accretion through channel A is also appreciable in more than the half of the total accretion period (type I). The circles denote those in which accretion through channel B is dominant for the total accretion period and the accretion through channel A is intermittent (type II).

The triangles denote those in which gas accretion is little ($\dot{M} < 0.02\dot{M}_{\text{inf}}$) in $2\pi \leq t \leq 12\pi$ (type III). All the models of $j_{\text{inf}} \geq 1.8$ show type III accretion. The boundary between type I and II depends on q . When q is larger, type I accretion takes place for a larger j_{inf} . When $q = 1$, type II accretion vanishes since the L2 and L3 points are identical. For later discussion we plot the specific angular momentum of a particle corotating with the binary at the L3 point, $j(\text{L3})$, with the dotted curve. The solid curve denotes $j(\text{L3}) + 0.11$. It is a good approximation to the boundary between type I and II. We plot the specific angular momentum of the particle corotating at L2 point with the dashed curve for comparison.

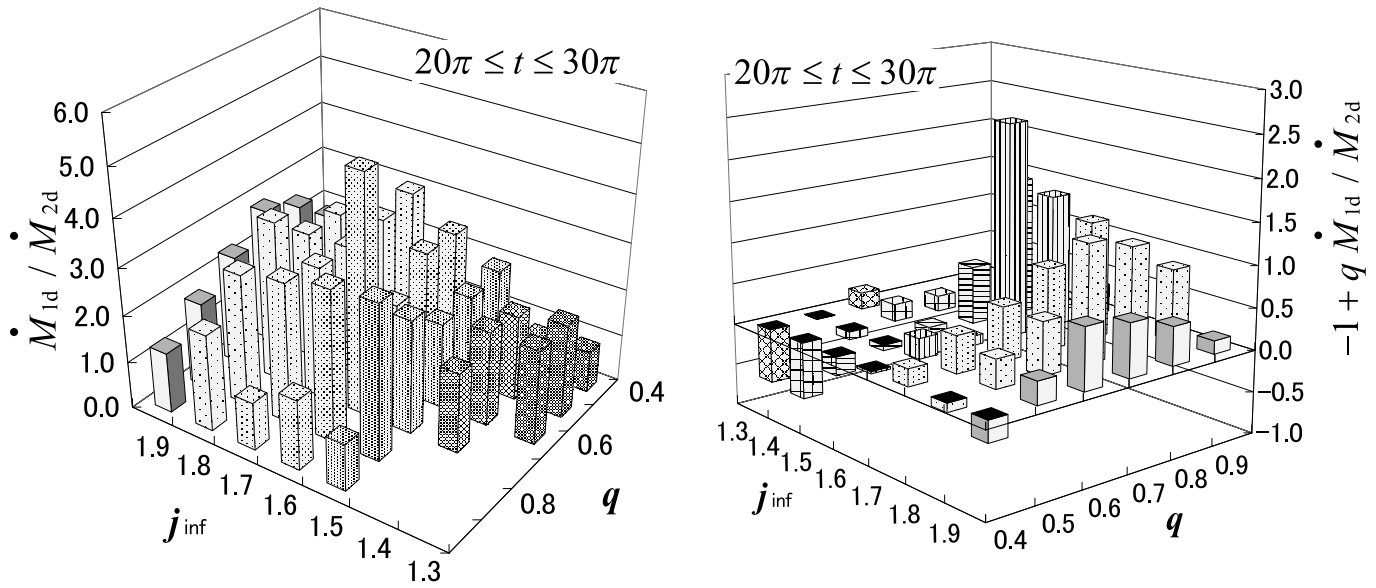


FIG. 14.—Dependence of the ratio of accretion rate $\dot{M}_{1d}/\dot{M}_{2d}$ on q and j_{inf} (left). The evolution of the mass ratio $-\dot{q} = \dot{M}_{2d}/M_1(-1 + q\dot{M}_{1d}/\dot{M}_{2d})$ is shown (right). Note that the bar height denotes the value of $-1 + q\dot{M}_{1d}/\dot{M}_{2d}$. Both panels denote the average accretion rates over the period $20\pi \leq t \leq 30\pi$. The cross-hatching denotes j_{inf} .

3.4. Dependence on the Sound Speed c_s

In this subsection we show models 6-19H, 6-19L, and 6-19LL. All these models, as well as model 6-19, have the same parameters, $q = 0.6$ and $j_{\text{inf}} = 1.9$, but different sound speed, c_s . The sound speed is $c_s = 0.30, 0.25, 0.20$, and 0.18 in models 6-19H, 6-19, 6-19L, and 6-19LL, respectively. Comparison of these models provides us dependence on c_s in type III accretion.

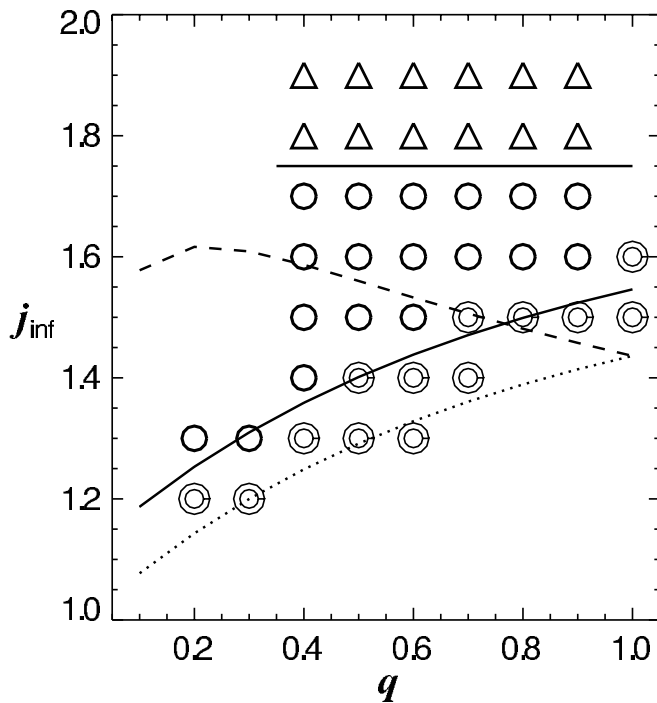


FIG. 15.—Classification of models on the mass ratio (q) and specific angular momentum of gas (j_{inf}) diagram. Type I accretion takes place in the models marked by the double circles, while type II accretion does in those marked by the single circles. Type III accretion takes place in the models marked by the triangles. See text for the definitions of types I, II, and III.

Figure 16 shows the surface density at $t = 10.0\pi$ in models 6-19H, 6-19, 6-19L, and 6-19LL. In model 6-19H the binary accretes gas appreciably at this stage, while it does not in the other three models. The circumbinary disks are detached from the binary in the latter three models. The spiral arms are thicker and more tightly wound in a model of a lower sound speed. This is reasonable, since the pitch angle of the spiral wave should be proportional to the ratio of the sound speed and rotation velocity (see, e.g., Roberts et al. 1975; Kennicutt 1981). When the sound speed is lower, the accreting gas spirals into the binary after a larger number of revolutions. The circumbinary disk is more extended and less dense in a model with a higher sound speed.

The left panel of Figure 17 shows the mass of the circumpriary disk as a function of time for models 6-19H, 6-19, 6-19L, and 6-19LL. The onset of the accretion is later in a model with a lower sound speed. This is because the spiral arms are tightly wound and the accreting gas comes close only a little by each rotation when the sound speed is low. After the onset, the accretion rate is nearly the same in all the models except for the very late phase in model 6-19LL.

The right panel of Figure 17 is the same as the left panel but for the mass of the circumsecondary disk. In the early phase, the accretion rate of the secondary is slightly higher in model 6-19H. In the late phase, however, it is high in model 6-19LL. The accretion onto the secondary begins around $t \simeq 12\pi$ in models 6-19, 6-19L, and 6-19LL.

Figure 18 summarizes the average accretion rate after the onset for models having $q = 0.6$ and $j_{\text{inf}} = 1.9$. Although the accretion rates of the primary and secondary disperse, they depend little on the sound speed.

3.5. On the Sporadic Variation

We examine the sporadic variation, which implies an uncontrolled process. A possible origin of the sporadic variation is poor resolution; our numerical solutions might contain numerical noise due to insufficient resolution.

As a convergence test, we have reexamined model 6-16 with different resolutions: 1024^2 , 2048^2 , 3072^2 , and 4096^2 grids. All the numerical solutions have converged in the early phase.

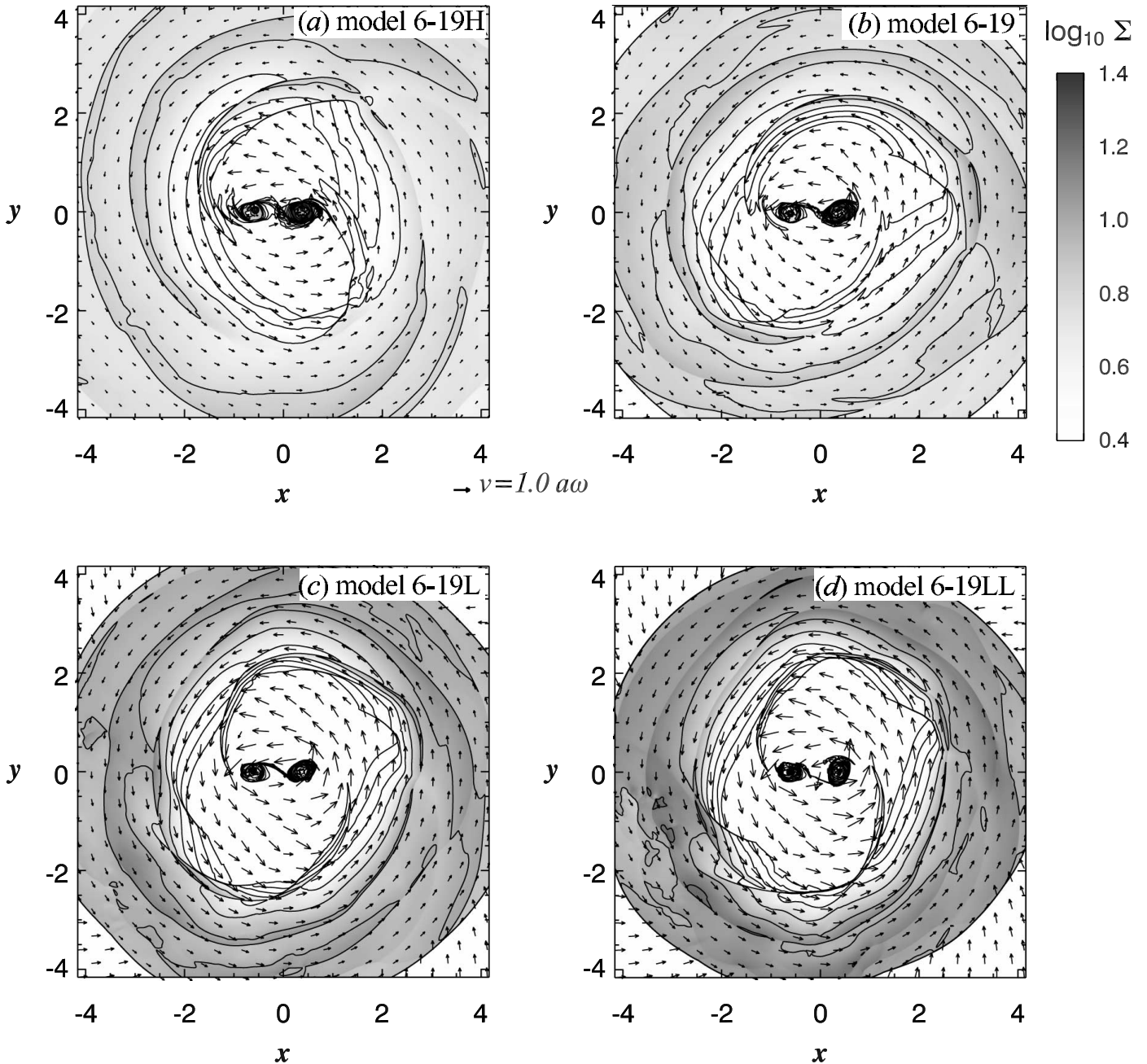


FIG. 16.—Dependence of accretion on the sound speed of gas, c_s . The panels denote the surface density and velocity measured in the rest frame at $t = 10\pi$ for models 6-19H, 6-19, 6-19L, and 6-19LL. The sound speed is $c_s = 0.30, 0.25, 0.20,$ and 0.18 , respectively.

Figure 19 compares the masses of the circumprimary and circumsecondary disks as a function of time for different resolutions. The masses are independent of resolution over the period $t \leq 2.8\pi$. The circumprimary and circumsecondary disks start accretion at $t = 2.4\pi$ and 2.6π , respectively.

At $t = 3\pi$, the mass of the circumprimary disk is slightly lower in the model with 1024^2 cells than in the others. On the other hand, the mass of the circumsecondary disk is slightly higher in the model with 1024^2 cells. These differences are due to numerical viscosity, which is larger in the computation of fewer cells. An appreciable fraction of the gas accretes from the circumprimary disk through the L2 point and directly onto the circumsecondary disk in the computation with 1024^2 cells. The direct accretion onto the circumsecondary disk is further enhanced in the computation of 512^2 cells, where the numerical

viscosity is larger. Thus, this direct accretion is due to the numerical viscosity. The numerical viscosity is estimated to be $\nu \approx \Delta x^2 / \Delta t$. Then the Reynolds number is evaluated to be

$$\begin{aligned} \text{Re} &= \frac{\ell v}{\nu} \\ &\approx \frac{a}{\Delta x} \frac{v \Delta t}{\Delta x} \\ &\approx 30 \left(\frac{N}{1024} \right), \end{aligned} \quad (13)$$

since the typical length scale is half of the binary separation, $0.5a$, in the Roche lobe and the Courant number is $v\Delta t/\Delta x = 0.6$. The flow is likely to be inviscid in our computations of

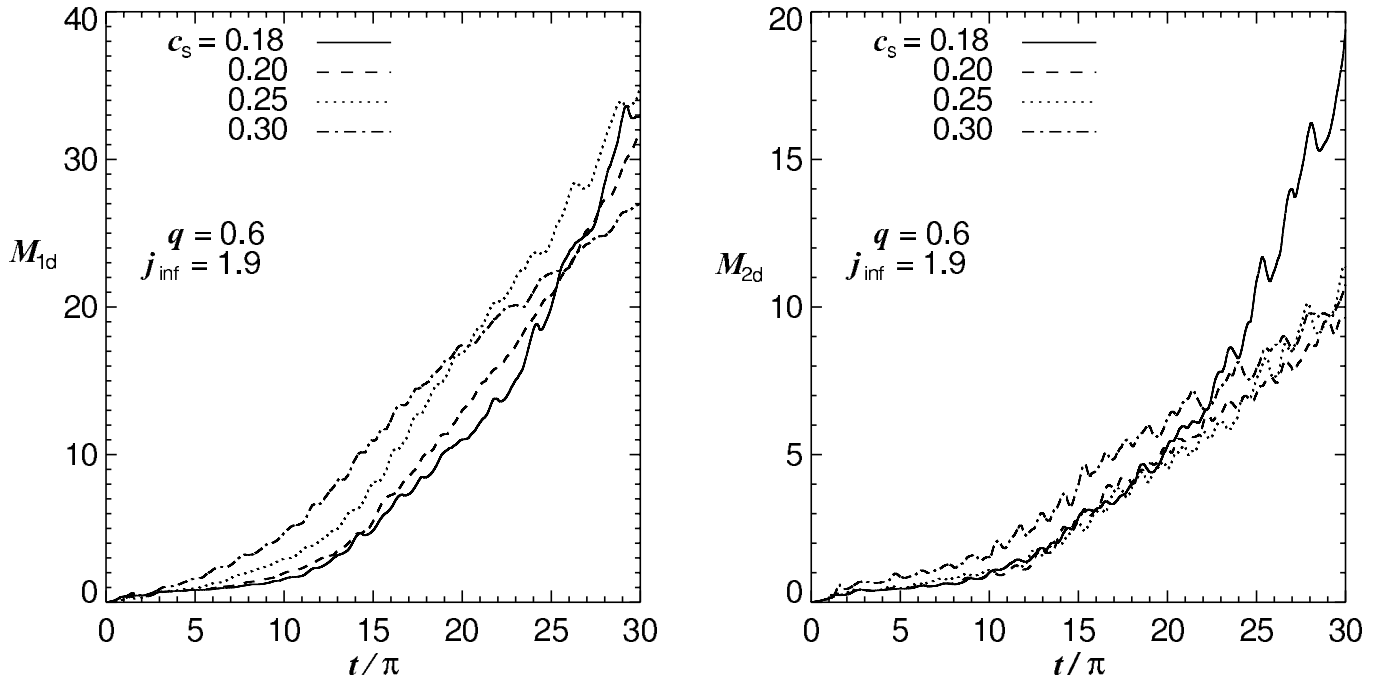


FIG. 17.—Solid, dashed, dotted, and dot-dashed curves denote M_{1d} (left) and M_{2d} (right) for models 6-19LL, 6-19L, 6-19, and 6-19H, respectively. Only the sound speed c_s is different between these models. The mass ratio and the specific angular momentum of the gas are the same ($q = 0.6$ and $j_{\text{inf}} = 1.9$).

$N \geq 2048$ (see Fig. 19). The masses of the circumprimary and circumsecondary disks depend little on the resolution except in the computation with 1024^2 cells over the period $t \leq 4\pi$.

Figure 20 is the same as Figure 19, but for the period of $0 \leq t \leq 30\pi$. The mass of the circumprimary disk is apprecia-

bly lower in the computation of 1024^2 cells after $t \gtrsim 14\pi$. This decrease is due to the numerical viscosity. The masses of the circumprimary and circumsecondary disks begin oscillation in the computation of 4096^2 cells around $t \simeq 20\pi$. The oscillation of M_{1d} anti-correlates with that of M_{2d} . The oscillation is due to instability of the stagnation point located near the L1 point. A small change in the stagnation point results in a large change in the destination of the flow, since the L1 point is the saddle point of the Roche potential. Thus, a large change in the circumprimary disk mass comes out from a small change in the stagnation point.

Figure 21 compares the computations of 2048^2 and 4096^2 cells for the flow near the L1 point at $t = 18.0\pi$ and 20.0π , respectively. The solid curves denote the streamlines and the plus signs indicate the stagnation point. The stagnation point at $t = 20.0\pi$ is located at $(x, y) = (-0.16, 0.04)$ and $(-0.20, 0.23)$ in the computations of 2048^2 and 4096^2 cells, respectively. The stagnation point is relatively stable in the computation of 2048^2 cells, while it is not in that of 4096^2 cells.

The instability of the stagnation point and the oscillation of the flow is explained as follows. The stagnation point moves by the balance between the dynamic pressures of the flows from the primary lobe and from the secondary lobe. When the flow from the primary lobe has a larger dynamic pressure, the stagnation point moves toward the secondary and the flow from the secondary lobe to the primary lobe diminishes. A smaller supply of gas from the secondary lobe lowers the dynamic pressure of the flow from the primary. As a result, the flow from the secondary lobe reopens and enters into the primary lobe through the L1 point. After rotating around the primary, the gas comes back to the L1 point. The period of oscillation is $\Delta t \simeq 2.4\pi$.

The average accretion rates are almost the same in the computations of 2048^2 , 3072^2 , and 4096^2 cells. The amplitude of the oscillation is the largest in the computation of 4096^2 cells, in which the Reynolds number is the highest. We suppose that the oscillation is damped numerically in the computation of a

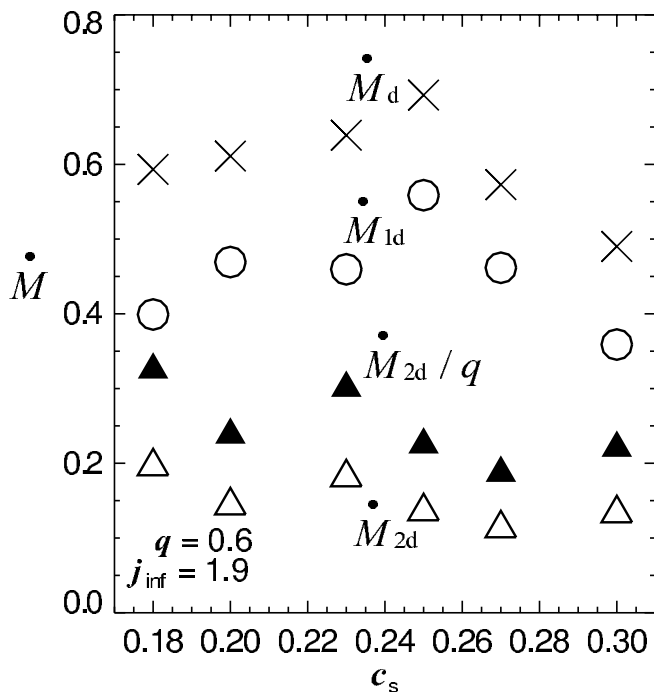


FIG. 18.—Dependence of the disk accretion rates on the sound speed, c_s . The mass ratio and the specific angular momentum of the accreting gas are fixed at $q = 0.6$ and $j_{\text{inf}} = 1.9$. The accretion rate is the average over the period $14\pi \leq t \leq 24\pi$. The open circles denote the accretion rate of the primary, \dot{M}_{1d} , and the open triangles do that of the secondary, \dot{M}_{2d} . The crosses denote the sum of them, \dot{M}_d , and the filled triangles denote \dot{M}_{2d}/q .

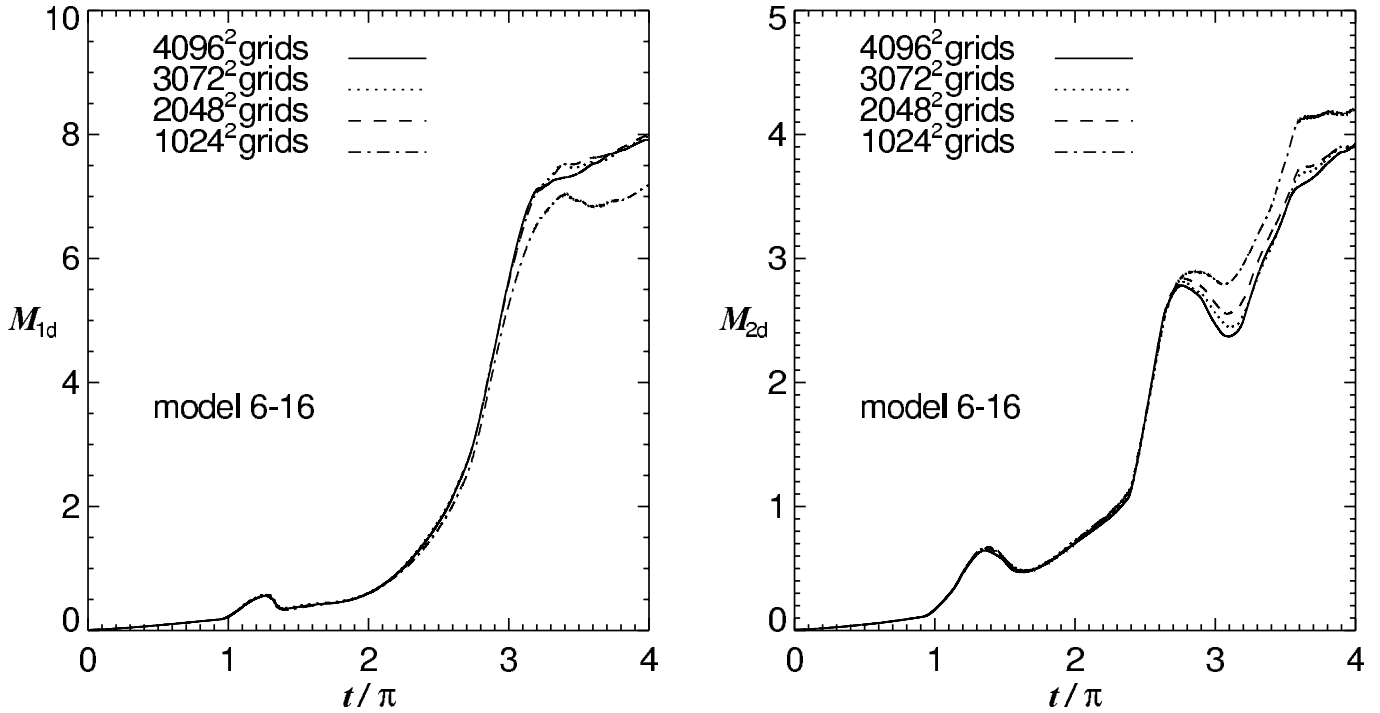


FIG. 19.—Dependence of the circumprimary disk mass, M_{1d} (left), and the circumsecondary one, M_{2d} (right), on the numerical resolution. The solid, dotted, dashed, and dash-dotted curves denote the disk masses for the grids 4096^2 , 3072^2 , 2048^2 , and 1024^2 , respectively. The mass ratio, the specific angular momentum, and the sound speed of gas are the same (model 6-16).

lower Reynolds number. The accretion rate shown in § 3 may suffer from the oscillation.

4. DISCUSSION

As shown in the previous section, the accretion rate varies both systematically and sporadically depending on the model parameters, j_{inf} , q , and c_s . We discuss the origins of these de-

pendences and then compare our simulations with the earlier simulations and observations thus far.

4.1. Dependence on j_{inf}

First, we discuss the increase in the accretion rate with time. The increase is remarkable especially in the models of $j_{\text{inf}} \geq 1.8$ (see Fig. 13). The increase in the accretion rate is stepwise (see

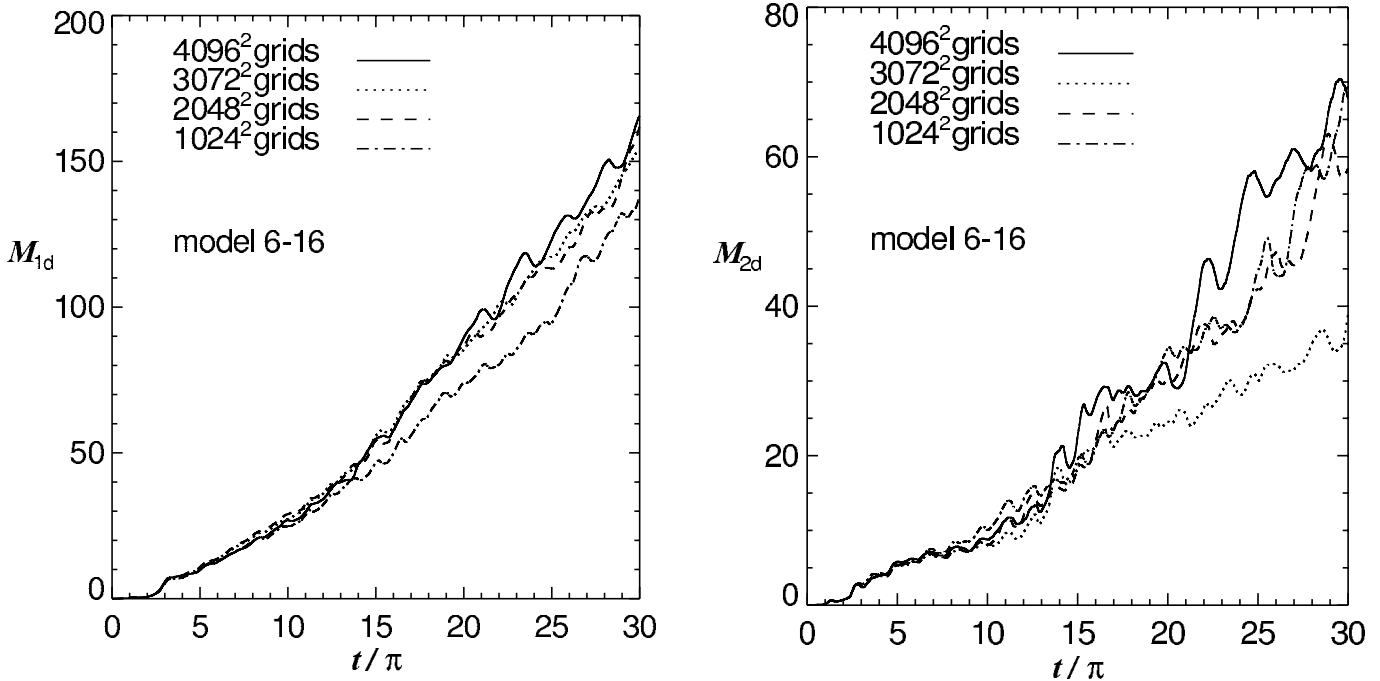


FIG. 20.—Same as Fig. 19 but for $0\pi \leq t \leq 30\pi$.

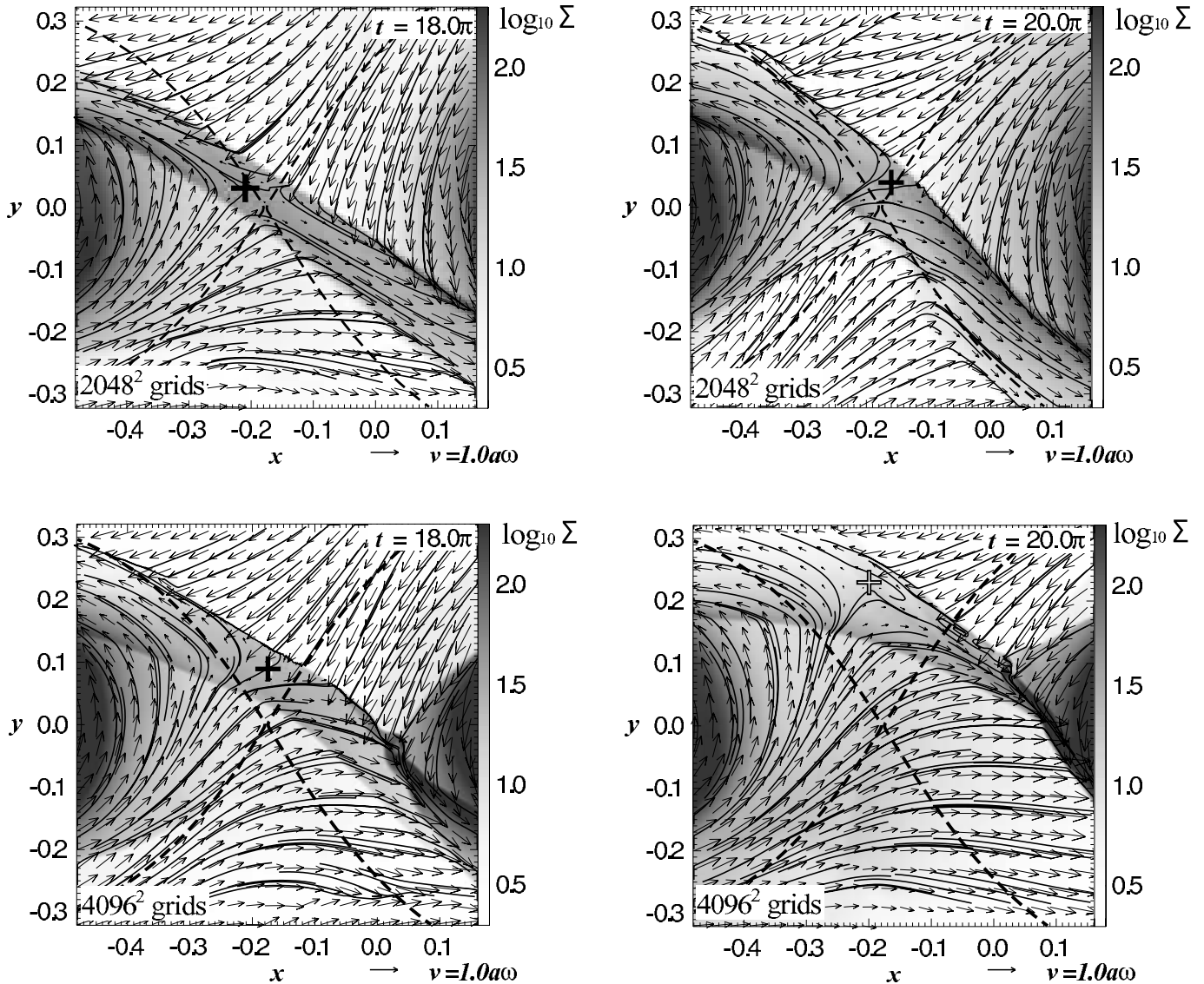


FIG. 21.—Streamlines (solid curves) overlaid on the surface density distribution (gray scale) near the L1 point. The left panels denote the stage of $t = 18.0\pi$ for model 6-16, while the right panels denote that of $t = 20.0\pi$. The spatial resolution is 2048^2 for the top panels and 4096^2 for the bottom panels. The plus sign denotes the stagnation point in each panel. The dashed curves denote the contour of the Roche potential passing through the L1 point.

Fig. 9). This implies two components in the gas accretion. One is absent in models of $j_{\text{inf}} \geq 1.8$, while the other appears in all the models but only in a late phase. We call the former and latter the fast and slow components, respectively. The increase in the accretion rate is ascribed to the spiral arms in the circumbinary disk in the models of $j_{\text{inf}} \geq 1.8$. The spiral arms transfer angular momentum outward and increase the accretion rate of the binary. This implies that the fast component of the accretion is due to another angular momentum transfer mechanism, i.e., the gravitational torque of the binary, while the slow component is due to the spiral waves.

The above argument is supported by a particle simulation. Nariai (1975) computed particles escaping from the L2 point with a small initial velocity and measured the specific angular momentum at the final state. The particles escaping from the L2 point have a specific angular momentum of $j_{\text{esc}} \simeq 1.7$ independently of q , and the initial small velocity assumed. This final specific angular momentum (j_{esc}) coincides with the critical specific angular momentum for the fast component of accretion ($j_{\text{inf}} \leq 1.7$). If the time is reversed, an escape particle is con-

verted into an accreting particle. Thus, particles of $j_{\text{inf}} = 1.7$ can reach the L2 point by gravitational force alone, since the particle orbit is time-reversible. Remember that this critical specific angular momentum is slightly larger than that for a particle corotating with the binary at the L2 point (see Fig. 15). The difference is ascribed to the angular momentum extraction by the gravitational torque. If we apply this argument to the L3 point, gas should accrete through the L3 point (channel A) when the specific angular momentum of infalling gas is slightly larger than that for a particle corotating at the L3 point, $j_{\text{inf}} < j(L3) + \delta$, where δ is nearly equal to 0.1. This argument is also consistent with Figure 15. The accretion onto the binary is discriminated into types I, II, and III at these two critical specific angular momenta.

4.2. Ratio of the Accretion Rates

As shown in the previous section, accretion through channel B (i.e., through the L2 point close to the secondary) is dominant over that through channel A in all the models of $j_{\text{inf}} \geq 1.3$. However, the accretion rate of the primary is larger than that of

the secondary ($\dot{M}_{1d} > \dot{M}_{2d}$) in all the computed models except for models 4-13 and 4-14 (see Fig. 14, *left panel*). The ratio of the accretion rates, $\gamma \equiv \dot{M}_{1d}/\dot{M}_{2d}$, is smaller than the inverse of the mass ratio, $1/q$, in most models (see Fig. 14, *right panel*). Then the gas accretion decreases the mass ratio in such models.

Our result is very different from that of Bate & Bonnell (1997); accretion increases the mass ratio in their simulations when $j_{\text{inf}} > 1.0$. They adopted a 3DSPH code to compute the accretion rate and assumed that all the injected gas particles have a given specific angular momentum, j_{inf} . When $1.2 \leq j_{\text{inf}} \leq 1.6$, gas accretes through the L2 point to the secondary irrespective of the mass ratio in their simulations.

We suppose that the accretion onto the secondary is due to the large numerical viscosity employed. When accreting gas flows near the L2 point, it should have an appreciable amount of energy and angular momentum, as shown in the previous section. It should lose energy and angular momentum before accreting onto either the primary or secondary. The sum of the Jacobi integral and the Gibbs free energy should be constant along the gas stream (Bernoulli's theorem; eq. [11]), if the flow is stationary in the corotation frame. The Gibbs free energy is much smaller than the Jacobi integral when the flow is cold. Thus, the Jacobi integral should be nearly constant along the streamline and for a given gas element. Unless energy is lost effectively, a gas element cannot accrete directly from the L2 point to the secondary, since the potential energy difference is very large compared with the thermal energy. We have confirmed that gas is also directly accreted onto the secondary in our simulations when the grid is coarse and hence the numerical viscosity is large (see § 3.5).

Our model is different from that of Bate & Bonnell (1997) at some points. Some of the differences other than the numerical viscosity might be responsible for the difference in the result. One of them is the treatment of the gas flow near the primary and secondary. Bate & Bonnell (1997) eliminated SPH particles when they fall within the accretion radius of the primary or secondary, whereas we have used the softened gravitational potential. The accretion radius is 5% of the binary separation ($r_{\text{acc}} = 0.05a$) in their simulations, while our model gravitational potential is softened in the regions of $|r - r_1| < 0.2a$ and $|r - r_2| < 0.2a$. The large softening radius might affect the flow inside the Roche lobe, although the inflow from the L2 point does not directly impact those softened regions in our simulations.

In order to assess the possible effects of large softening radius, we have made comparative models of $R_1 = R_2 = 0.15a$ for model 6-16 with 6144² cells (model 6-16a) and 8192² cells (model 6-16b). The mass ratio, the specific angular momentum of the infalling gas, and the sound speed are set equal to those of model 6-16. The flow outside the Roche lobe is almost the same among models 6-16, 6-16a, and 6-16b. The average accretion rates of the primary and secondary differ from model to model. They are $\dot{M}_{1d} = 2.51$ and $\dot{M}_{2d} = 2.98$ in the model 6-16a over the period $20\pi \leq t \leq 30\pi$, whereas they are $\dot{M}_{1d} = 2.38$ and $\dot{M}_{2d} = 1.95$ in the same period in model 6-16b. The accretion rate of the secondary is appreciably higher in model 6-16a than in model 6-16b. This is due to relatively large viscosity in model 6-16a. Since the effective radii are small in models 6-16a and 6-16b, the maximum velocity is larger than in model 6-16 and the time step (Δt) is taken to be shorter. Consequently the numerical viscosity is large in model 6-16a despite the very high resolution. Thus, our result that the primary accretes more than the secondary is not due to the softening employed.

It is enlightening to compare the numerical viscosity with the standard α viscosity. The former is $\nu \approx (\Delta x)^2/\Delta t \approx 1.67v_{\text{max}}\Delta x$ in terms of the kinetic viscosity while the latter is $\nu \approx \alpha c_s H$,

where H denotes the disk thickness. They are evaluated to be $\nu \approx 7.4 \times 10^{-2} \alpha c_s$ and $8.8 \times 10^{-3} \alpha c_s$ for the numerical viscosity and α viscosity, respectively, in model 6-16 when computed with 2048² cells. Thus, the numerical viscosity is much larger than the turbulent viscosity expected from the standard theory even when c_s is rather high. If we take account the turbulent viscosity, the flow will gain a small radial drift velocity, $v_r \approx \alpha c_s^2/v_\phi$ (see, e.g., Frank et al. 1985; Hartmann 1998). Since the drift velocity is much smaller than the rotation velocity, it is unlikely that the gas inflowing through the L2 point accretes directly onto the secondary. It should flow toward the L1 point, as shown in our simulations.

It is possible for the secondary to capture the inflow directly if it is large and comparable with the Roche lobe, i.e., $R_2 \gtrsim 0.3a$. This can happen only for a very short period binary. Suppose that the radius of the secondary is 10 times larger than the Sun ($R_1 = 10 R_\odot$) and the masses of the primary and secondary are $M_1 = 0.625 M_\odot$ and $M_2 = 0.375 M_\odot$. Then the orbital period of the binary is 23 days when $R_2 = 0.3a$. Thus, the secondary is much smaller than the Roche lobe in most binaries since this period is very short.

It is interesting to compare our simulations with those of Günther & Kley (2002). They modeled four binaries, AK Sco, DQ Tau, UY Aur, and GG Tau. All of them have appreciable eccentricities ($0.13 \leq e \leq 0.56$). AK Sco and DQ Tau are close binaries, while UY Aur and GG Tau are wide binaries. They assumed a geometrically thin, coplanar, circumbinary disk in Keplerian rotation and computed accretion onto the binary in the orbital plane. They found that the accretion rate of the primary is larger than the secondary in three out of the four models. Their figures show a sharp bridge near the L1 point, which indicates mass exchange between the primary and secondary lobes. They adopted a dual-grid technique to achieve high spatial resolution around the binary. This supports our results in the sense that high spatial resolution results in higher primary accretion rates.

As mentioned earlier, our models predict that gas accretion increases the mass difference between the primary and secondary, since the primary accretion rate is higher than the secondary one in almost all the models. Not only the absolute accretion rate, but also the accretion rate per unit mass (\dot{M}/M), is higher for primaries in most models.

The ratio of the primary and secondary accretion rates depends little on the initial infall velocity, v_{inf} . We have made model 6-16c, whose parameters are the same as those of model 6-16 except v_{inf} . The initial infall velocity is twice as large in model 6-16 as in model 6-16c. Consequently the average accretion rate is 50% higher in model 6-16. The total accretion rate is $\dot{M}_{1d} + \dot{M}_{2d} = 3.45$ over the period $20\pi \leq t \leq 30\pi$ in model 6-16, while it is $\dot{M}_{1d} + \dot{M}_{2d} = 2.26$ in the same period in model 6-16c. The branching ratio, $\dot{M}_{1d}/\dot{M}_{2d}$, is nearly the same; it is 2.51 and 2.44 in models 6-16 and 6-16c, respectively. This is further evidence that the ratio of the accretion rates depends on the flow inside the Roche lobe.

4.3. Comparison with Young Close Binaries

Our numerical simulations are aimed to model a protobinary in the main accretion phase. It is deeply embedded in a molecular cloud, and the components are hard to distinguish. Thus, we compare our simulations with close binaries of classical T Tauri stars. They are a little evolved and have slightly lower accretion rates. Hence, each component can be discriminated and is easier to compare with our simulations.

Hartigan & Kenyon (2003) obtained Space Telescope Imaging Spectrograph spectra for 20 close T Tauri binaries in the

Taurus-Auriga dark cloud. They derived mass accretion rates and other stellar parameters from the spectra. According to them, the primaries tend to have somewhat larger accretion rates than their secondaries do. They also found four mixed pairs of classical T Tauri and weak-lined T Tauri stars. The primary is the classical T Tauri in three out of the four pairs. It is another evidence that a primary tends to have a larger accretion rate.

The apparent separation is less than an arcsecond in most of these binaries. This means that the typical separation is less than 100 AU and the specific angular momentum of the binary is small. Accordingly, the gas accreted onto the binary is likely to have had a large specific angular momentum when measured in units of the binary specific angular momentum. In this sense our simulations are consistent with those of Hartigan & Kenyon (2003).

4.4. Implication for Mass Ratio Distribution

As shown in the previous section our computations have shown that the primary has a larger accretion rate and accordingly the mass ratio decreases. We consider the implication for the mass ratio distribution.

According to recent surveys (Köhler & Leinert 1998; Köhler et al. 2000; Woitas et al. 2001; White & Ghez 2001; Patience et al. 2002), the mass ratio distribution is flat in the range of $q \geq 0.2$ except for the detection bias. This implies that the primary tends to have a slightly higher accretion rate. If the secondary had a higher accretion rate, the mass ratio would increase by accretion and the mass ratio distribution would have a sharp peak near $q \simeq 1$. On the contrary, low mass ratio binaries would become more abundant if the mass ratio decreased rapidly by accretion. Thus, the flat distribution implies that accretion decreases and disperses the mass ratio slowly. In this sense our simulations are consistent with the mass ratio distribution.

4.5. Unresolved Issues

We adopted a very simple model in this paper; we assumed a circular orbit, coplanar gas accretion, constant sound speed, and so on. This simple model enabled us to achieve high spatial resolution and hence high Reynolds number. We should, however, remember the shortcomings of this simple model. We assess these shortcomings in this subsection.

When the binary has an eccentric orbit, the separation changes periodically and the accretion rate changes accordingly (Artymowicz & Lubow 1996). The Roche lobe repeats expansion and contraction synchronized with the orbital motion. Then the gas flow into the Roche lobe should be larger at the apocenter than at the pericenter. In addition, the accretion rates of the primary and secondary should vary synchronously. The ratio of \dot{M}_{1d} to \dot{M}_{2d} should vary, and the average ratio may depend on the eccentricity. Accretion onto an eccentric binary is beyond the scope of this paper and an open problem. It should be investigated with future simulations of high resolution.

The assumption of a coplanar circumbinary disk seems to be reasonable as far as binaries are concerned. Observed circumbinary rings seem to be coplanar with the binary located in the central hole. However, we should remember that an appreciable fraction of stars belong to hierarchical triplets and quadruples. The outermost member of the multiple may not be coplanar with the central pair, since it is highly likely to be scattered by gravitational interaction. It may disturb the circumbinary disk around the central pair. Effects of the third body are beyond the scope of this paper.

Our numerical simulations might depend on the adopted sound speed of the gas. For simplicity we assumed that the sound

speed of the gas is constant in the range $0.18a\omega \leq c_s \leq 0.30a\omega$. The assumed sound speed is a little higher than a realistic value. The unit velocity and the sound speed are evaluated to be

$$a\omega = 2.97 \left(\frac{M}{0.1 M_\odot} \right)^{1/2} \left(\frac{a}{10 \text{ AU}} \right)^{-1/2} \text{ km s}^{-1} \quad (14)$$

and

$$c_s = 0.19 \left(\frac{T}{10 \text{ K}} \right)^{1/2} \text{ km s}^{-1}. \quad (15)$$

Of course these numbers may change from binary to binary and should evolve with time. The gas temperature may increase, since radiation from the protobinary may heat up the surrounding gas.

We have chosen the value of $c_s/(a\omega)$ mainly for a technical reason. When c_s is smaller, the computation requires higher spatial resolution and accordingly takes more computation time. Although we have assumed a rather high sound speed, our conclusion depends only weakly on the sound speed as long as the flow is relatively cold. As shown in § 3, the ratio of the accretion rates depends mainly on the flow within the Roche lobe. The gas pressure has only minor effects on the flow. The Roche potential is $\phi(\text{L2}) = -1.77$, $\phi(\text{L1}) = -1.99$, and $\phi(\text{L3}) = -1.68$ at the three Lagrange points, respectively, for $q = 0.6$, while $c_s^2 = 0.0625$. In fact, the accretion rates of the primary and secondary depend little on the sound speed in the range we have investigated.

5. SUMMARY

As shown and discussed earlier, the accretion rate of the primary is larger than that of secondary, even when the accreting gas has a large specific angular momentum. This conclusion contradicts the simulations of Bate & Bonnell (1997), which have been regarded as a standard. The difference comes mainly from their large numerical viscosity. Very high spatial resolution and low numerical viscosity are essential for simulating the flow inside the Roche lobe and for evaluating the accretion rate of each component star. It has been believed thus far that the primary accretes more than the secondary only when the accreting gas has a low specific angular momentum. Our simulations have refuted this belief. Gas accretion tends to increase the mass difference and hence to decrease the mass ratio.

The gas accretion onto the binary consists of fast and slow components. The former is significant only when $j_{\text{inf}} \leq 1.7$, i.e., when the accreting gas has a specific angular momentum smaller than the critical value. The critical value depends little on the mass ratio, q . The slow component is due to spiral shock waves in the accretion flow. When the sound speed is lower, the slow component begins later. The accretion rate of the slow component depends little on the sound speed.

We thank T. Matsumoto and N. Fukuda for their useful comments and providing us with visualization tools. We are also grateful to S. Ikeuchi, R. Matsumoto, S. Miyaji, and T. Matsubara for their advice and encouragement. We also thank an anonymous referee for his/her comments on the early version of the manuscript. Numerical simulations have been performed on Fujitsu VPP5000 at the Astronomical Data Analysis Center of the National Astronomical Observatory, Japan (myo79c, yyo30b, and ryo01b). This study is financially supported in part by the Grant-in-Aid for Scientific Research (B)(15340062) of the Japan Society for the Promotion of Science (JSPS).

REFERENCES

- Artymowicz P. 1983, *Acta Astron.*, 33, 223
Artymowicz, P., & Lubow, S. H. 1996, *ApJ*, 467, L77
Bate, M. R. 1997, *MNRAS*, 285, 16
Bate, M. R., & Bonnell, I. A. 1997, *MNRAS*, 285, 33
Close, L. M., et al. 1998, *ApJ*, 499, 883
Duvert, G., Dutrey, A., Guilloteau, S., Menard, F., Schuster, K., Prato, L., & Simon, M. 1998, *A&A*, 332, 867
Frank, J., King, A. R., & Raine, D. J. 1985, *Accretion Power in Astrophysics* (Cambridge: Cambridge Univ. Press)
Günther, R., & Kley, W. 2002, *A&A*, 387, 550
Hartigan, P., & Kenyon, S. J. 2003, *ApJ*, 583, 334
Hartmann, L. 1998, *Accretion Processes in Star Formation* (Cambridge: Cambridge Univ. Press)
Hirsch, C. 1990, *Numerical Computation of Internal and External Flows*, Vol. 2 (Chichester: Wiley)
Kennicutt, R. C., Jr. 1981, *AJ*, 86, 1847
Köhler, R., Kunkel, M., Leinert, C., & Zinnecker, H. 2000, *A&A*, 356, 541
Köhler, R., & Leinert, Ch. 1998, *A&A*, 331, 977
Larson, R. B. 2003, *Rep. Prog. Phys.*, 66, 1651
Mathieu, R. D., Ghez, A. M., Jensen, E. L. N., & Simon, M. 2000, in *Protostars and Planets IV*, ed. V. Mannings, A. P. Boss, & S. S. Russell (Tucson: Univ. Arizona Press), 703
Nariai, K. 1975, *A&A*, 43, 309
Patience, J., Ghez, A. M., Reid, I. N., & Matthews, K. 2002, *AJ*, 123, 1570
Roberts, W. W., Jr., Roberts, M. S., & Shu, F. H. 1975, *ApJ*, 196, 381
Roddier, C., Roddier, F., Northcott, M. J., Graves, J. E., & Jim, K. 1996, *ApJ*, 463, 326
Roe, P. L. 1981, *J. Comput. Phys.*, 43, 357
White, R. J., & Ghez, A. M. 2001, *ApJ*, 556, 265
Woitas, J., Leinert, Ch., & Köhler, R. 2001, *A&A*, 376, 982